Integrated Electrochemical and Machine Learning Framework for $SiO_2/CaCO_3$ Under-deposits Driven Welded X65 Carbon Steel Corrosion Mitigation in Sour Service Conditions

Adewale K. Ipadeola[1*], Mostafa H. Sliem[1], Dana Abdeen[2], Nicholas Laycock[2], Ashwin RajKumar[3], Phaneendra K. Yalavarthy[3*], Aboubakr M. Abdullah[1*]

[a]Center for Advanced Materials, Qatar University, Doha 2713, Qatar

[b]Qatar Shell Research and Technology Centre, P.O. Box 3747, Doha, Qatar

[c]Department of Computational and Data Sciences (CDS), Indian Institute of Science (IISc), Bangalore, India.

[*]Corresponding author: ak.ipadeola@qu.edu.qa; yalavarthy@iisc.ac.in; bakr@qu.edu.qa

Abstract

The integrity of welded X65 carbon steel (CS) pipelines in oil and gas systems is significantly compromised by preferential weldment corrosion (PWC) and pitting in sour conditions. This study clarifies that the effect of pre-corrosion conditioning and inorganic deposits (SiO_2 or $CaCO_3$) on welded CS pipelines, with SiO_2 deposits leading to the most substantial damage at weld metal (WM) and heat-affected zone (HAZ) relative to parent metal (PM). Due to localized acidification and differences in potential, corrosion rates (CRs) hierarchies are SiO_2-deposited > $CaCO_3$-deposited > non-deposited. Microstructural analysis revealed that deposited CS-WM had carbide redistribution and increased residual stress from the welding thermal process, with increased aggressive species and stabilized iron oxides, leading to intensified PWC. However, amine-based inhibitor CRW11 suppressed the CRs below 0.1 mmpy through chemisorbed films that disrupted microgalvanic coupling and protective corrosion product layers with inhibition efficiency (IE > 85%). CS-PM-$CaCO_3$ had a high pit depth (68.3 ± 2.7 μm) and propagation rate (1.2 ± 0.2 mmpy), making it the most vulnerable region to pitting relative to CS-WM-$CaCO_3$ (52.5 ± 1.1 μm; 0.9 ± 0.1 mmpy) and CS-HAZ-$CaCO_3$ (29.3 ± 0.6 μm; 0.5 ± 0.1 mmpy). This proves that $CaCO_3$ deposit on welded CS created a physical barrier for the surface nucleation effect and improved anodic dissolution. Machine learning models (Random Forest (RF), Decision Tree (DT), Gradient Boost (GB), and Extreme Gradient Boost (XGBoost)) accurately predicted IE (R^2 = 0.99). However, RF performed best without deposits (RMSE = 0.9), while DT yielded the lowest errors with SiO_2 and $CaCO_3$ deposits (RMSE = 0.5 and 0.2). These findings provide coupled electrochemical,

microstructural, and machine learning frameworks for PWC mitigation, allowing for adaptive corrosion management methods in sour service pipes and material designs optimized for topology.

Keywords: Under-deposited welded carbon steel; Sour media corrosion tests; Microstructural alterations; Pit depth/densities; Random forest/Decision tree.

1. Introduction

Critical integrity risks in oil and gas facilities, particularly welded X65 carbon steel (CS) pipelines, are mainly caused by preferential weld corrosion (PWC) and pitting corrosion under sour conditions present. These are driven by synergistic interactions between microstructural gradients, deposit types, environmental chemistry, and hydrodynamic conditions (Adegbite, 2014; Niu et al., 2024; Sun et al., 2022). PWC manifests through galvanic potential disparities between the parent metal (PM), weld metal (WM), and heat-affected zone (HAZ), arising from compositional and microstructural heterogeneities introduced during welding processes (Aljohani et al., 2023; Lahiri, 2017; Nofrizal et al., 2016). In sour environments containing CO_2 and H_2S, these disparities are amplified by the formation of inorganic scales or deposits (e.g., $FeCO_3$, FeS_x) that promote localized acidification through under-deposit corrosion mechanisms (Abdullah et al., 2025; Case et al., 2015). Operational dynamics further complicate degradation processes, where turbulent flow regimes exceeding 10 m/s disrupt protective corrosion inhibitor films through shear stress, triggering galvanic current reversals that accelerate WM/HAZ dissolution (Adegbite, 2014; Alawadhi and Robinson, 2011). Cyclic variations in temperature and hydrodynamic shear create metastable interfaces, alternating between active anodic dissolution and transient passivation phases. For instance, a recent study demonstrated high-velocity flows (>10 m/s) that removed protective $FeCO_3$ layers on WM surfaces, exposing reactive substrates to corrosive brines while maintaining cathodic protection on PM regions (DA SILVA, 2023). This flow-induced differential passivation establishes macro-galvanic couples with area ratios exceeding 100:1 (PM:WM), exponentially increasing localized corrosion rates (CRs) through mixed potential theory mechanisms (Tan, 2022). The complexity is intensified by H_2S-induced hydrogen embrittlement in WM regions, which synergizes with galvanic effects to promote subsurface crack initiation beneath corrosion product layers (Behvar et al., 2024; Li et al., 2021; Martin and Sofronis, 2022).

These studies highlight the importance of thoroughly understanding corrosion mechanisms under realistic and dynamic conditions in oil and gas facilities.

An effective strategy for mitigating corrosion of welded CS is the use of corrosion inhibitors, but their performance is influenced by various environmental and operational factors (Aslam et al., 2022; Aydinsoy et al., 2024; Răuță et al., 2025). For instance, nonanedihydrazide inhibitor displayed high IE (~98.3%) for mild CS in 1M HCl by chemically adsorbing onto the surface via Langmuir's isotherm model (Al-Amiery et al., 2022). However, its efficacy decreased with increasing temperature, emphasizing the sensitivity of adsorption mechanisms to thermal conditions. Similarly, 2-thiobarbituric acid (TBA) exhibited IE (> 90%) for API X60 steel in CO_2-saturated NaCl solutions across a range of pH levels and immersion times, with its performance governed by chemical adsorption and concentration-dependent behavior (Usman et al., 2019). The effectiveness of inhibitors like VpCI-A and VpCI-B in dynamic systems was shown to depend on flow rates and concentration adjustments, as higher flow rates increased CRs requiring enhanced inhibitor dosages (Miksic et al., 2009). These findings underscore the critical role of adsorption behavior, environmental parameters (e.g., pH, temperature), and operational dynamics in determining the reliability of corrosion inhibitors under varying conditions.

Latest investigations have emphasized the critical influence of pre-corrosion surface conditions and the morphology of conductive deposits on the initiation and progression of corrosion processes (Pessu et al., 2022; Xu et al., 2020; Zhang et al., 2024). Advanced surface characterization methods (i.e., scanning electron microscopy (SEM) and energy-dispersive X-ray spectroscopy (EDS)) have revealed that pre-existing corrosion products significantly affect the nucleation and growth of silica (SiO_2) and calcium carbonate ($CaCO_3$) deposits, contributing to localized electrochemical cells with intensified cathodic activity (Dwivedi et al., 2017; Yang, 2020). This underscores the intricate interplay between surface chemistry, microstructural features, and environmental variables in determining corrosion mechanisms. However, achieving a comprehensive mechanistic understanding remains challenging due to the limited integration of electrochemical, microstructural, environmental factors, and machine learning (ML) algorithms in current research frameworks. The complexity is particularly evident in welded joints exposed to sour media, where alternating phases of active corrosion and inhibitor protection generate metastable interfaces. These dynamic systems, deepened by heterogeneous microstructural distributions and localized electrochemical activity, pose substantial obstacles to accurately

predicting and mitigating corrosion phenomena in oil and gas industries (Abdulstaar et al., 2013; Paolinelli et al., 2008).

ML algorithms have significantly advanced corrosion prediction and inhibitor optimization by overcoming limitations of conventional models, which struggle to account for multivariate interdependencies and complex environmental factors (Fayyad et al., 2025). For instance, random forest (RF) algorithms proved high accuracy in predicting soil-buried steel CRs, achieving minimal root mean square error (*RMSE*) by incorporating variables such as moisture content, pH, chloride concentration, and total organic carbon into their ensemble-based approach (Dong et al., 2024). Similarly, multilayer perceptrons (MLPs) excel in modeling CO_2-induced corrosion by abstracting hierarchical relationships between environmental parameters, achieving predictive performance with coefficient of determinant (R^2) values exceeding 0.95 (Ruiz et al., 2024). In industrial cooling systems, dense neural networks proved effective as virtual sensors for estimating CRs, yielding mean absolute percentage errors (*MAPE*) of 25% and 11% for direct and indirect circuits, respectively. Additionally, convolutional neural networks (CNNs) and long short-term memory (LSTM) networks showed superior accuracy in temporal CRs prediction for pipelines, with low *MAPE* of 4 and 9%, respectively, depending on circuit type (Ruiz et al., 2024). Beyond prediction, ML models, like artificial neural networks (ANNs), have optimized inhibitor formulations by mapping chemical descriptors to adsorption energy and charge transfer resistance, enabling tailored strategies for specific operational conditions (Coelho et al., 2022; Nguyen et al., 2022). These advancements underscore the transformative potential of ML in corrosion science, offering robust tools for accurate predictions and resource-efficient protective measures across diverse material systems and environments.

This study advances corrosion science by employing a multi-technique approach that integrates electrochemical analysis, surface characterization, and ML algorithms to investigate corrosion mechanisms in preconditioned X65 weldments with inorganic deposits (SiO_2 and $CaCO_3$). Realistic sour service environments were simulated using sodium thiosulfate ($Na_2S_2O_3$), acetic acid (CH_3COOH), and CO_2 gas to analyze localized attack propagation. It is permissible and occasionally beneficial to substitute $Na_2S_2O_3$ and CH_3COOH for H_2S, particularly for better handling, safety, and in-situ controlled release of H_2S. Also, this substitute's significant mechanistic discoveries are widely reported in the literature, with equivalent effects on corrosion quantification related to direct H_2S exposure (Baranwal and Rajaraman, 2019; Kappes et al., 2012;

Samusawa et al., 2025; Talukdar and Rajaraman, 2020). The performance of an amine-based corrosion inhibitor (CRW11) for controlled corrosion inhibition without/with conductive SiO_2 or $CaCO_3$ deposits on the welded CS. Artificial pit growth measurements, achieved by one-dimensional (1D) artificial pit techniques and Raman spectroscopy, provide critical insights into pitting and corrosion products evolution. The incorporation of predictive ML algorithms utilizing comprehensive input parameters marks a paradigm shift in corrosion management strategies, enabling proactive risk assessment for welded infrastructure in complex operational environments.

2. Materials and methods

2.1 Materials and reagents

Chemicals of analytical grade were obtained from Sigma Aldrich (St. Louis, MO, USA), including sodium chloride (NaCl), sodium thiosulfate ($Na_2S_2O_3$), isopropanol (C_3H_7OH), acetone ($(CH_3)_2CO$), acetic acid (CH_3COOH), Nafion solution, and carbon dioxide (CO_2) gas. Additional materials included Milli-Q water, polishing pads, and laboratory inorganic deposits such as silicon dioxide (SiO_2) and calcium carbonate ($CaCO_3$). X65 welded carbon steel pipeline material was supplied by Qatar Shell, while a commercial amine-based corrosion (CRW11) inhibitor was sourced from Baker Hughes.

2.2. X65 Carbon steel coupon machining, polishing, and pre-conditioning method

Cylindrical specimens (5 × 60 mm) were extracted from the PM, WM, and HAZ regions of an X65-grade welded CS pipeline, oriented perpendicular to the pipeline axis. The samples underwent sequential polishing to achieve a mirror finish using abrasives ranging from 220 to 2000 grit. Subsequently, the polished coupons were cleaned with deionized water and isopropanol before being stored in a controlled environment (**Fig. 1a**). A 1.0 wt.% NaCl solution was deoxygenated by purging with nitrogen gas for 2 h under agitation.

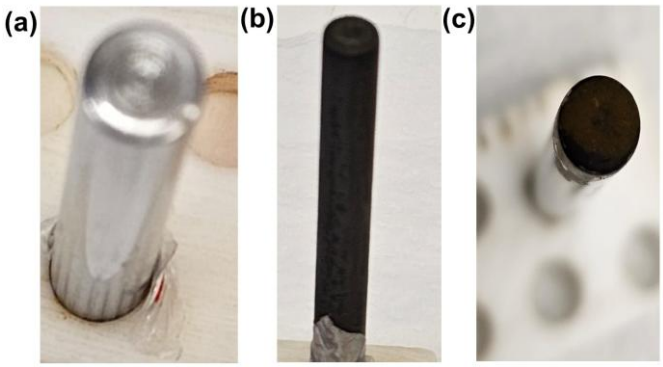

Fig. 1: (a) Polished X65 CS, (b) preconditioned X65 CS in sweet media, and (c) Deposited X65 CS after preconditioning.

The polished welded CS specimens were then immersed in this solution within an autoclave, pressurized to 40 psi with CO_2, and maintained at 50 °C for 1.5 h. This treatment facilitated the formation of a uniform, greyish protective scale on the X65 welded carbon steel surfaces (**Fig. 1b**), predominantly composed of iron oxides rather than iron carbonate ($FeCO_3$), due to the thermodynamic stability of iron oxides in chloride-rich environments. Corrosion analysis was performed immediately following this preconditioning process.

2.3. Deposit ink preparation

Synthetic pipeline inorganic deposits (SiO_2 and $CaCO_3$) were replicated under controlled laboratory conditions. Specifically, 300 mg each of SiO_2 and $CaCO_3$ were suspended in a mixture of isopropyl alcohol and Nafion, followed by sonication to ensure uniform dispersion. The resulting suspensions were applied onto X65 welded CS rod substrates and subjected to a two-stage drying protocol: initial air-drying for 2 h and subsequent oven treatment at 80 °C for 4 h. This methodology yielded adherent films that covered approximately 75% of the substrate surface (**Fig. 1c**), effectively simulating real-world pipeline deposit formations.

2.4. Sample and electrolyte preparation for corrosion tests

X65 welded CS cut from PM, WM, and HAZ regions were prepared for corrosion testing. The samples were mounted in epoxy resin to expose a controlled surface area (0.2 cm^2) and underwent degreasing, rinsing, and preconditioning procedures. Electrochemical experiments were conducted in a simulated sour environment comprising 3.5 wt.% NaCl, 1000 ppm $Na_2S_2O_3$, and 100 ppm CH_3COOH, with CO_2 purging at 60 °C and stirring at 1000 rpm. Sodium thiosulfate ($Na_2S_2O_3$) and

acetic acid (CH_3COOH) were used as substitutes for hydrogen sulfide (H_2S) to ensure safety during testing. This experimental setup allowed precise control over environmental parameters, effectively simulating operational pipeline conditions for evaluating corrosion behavior and inhibitor performance.

A commercially available amine-based corrosion inhibitor, CRONOX-CRW85711 (designated as CRW11), was introduced into a glycol-aqueous solution at a concentration of 200 ppm. To simulate dynamic flow conditions typical of industrial sour service environments, specimens were affixed to a rotating electrode assembly operating at 1000 rpm. This experimental configuration ensured consistent hydrodynamic conditions and reproducibility, aligning with established industrial protocols for evaluating material performance under sour conditions.

2.5. Electrochemical measurements

Electrochemical corrosion measurements were performed using a GAMRY 3000 potentiostat, incorporating open circuit potential (OCP), electrochemical impedance spectroscopy (EIS), linear polarization resistance (LPR), and electrochemical noise (EN) techniques. The experimental setup utilized a three-electrode double-jacketed cell equipped with temperature control. A welded X65 carbon steel rod functioned as the working electrode, while an Ag/AgCl electrode saturated with KCl served as the reference electrode, and a graphite rod was employed as the counter electrode. Tests were conducted under simulated sour conditions comprising 3.5 wt.% NaCl, 1000 ppm $Na_2S_2O_3$, 100 ppm CH_3COOH, CO_2 saturation at 60°C with a stirring rate of 1000 rpm and a pH of approximately 4. EIS measurements were carried out over a frequency range of 0.1 Hz to 100 kHz using an AC amplitude of 10 mV, followed by LPR and electrochemical noise (EN) analyses. Triplicate experiments were measured to ensure reproducibility and reliability. EIS data were modeled using Voigt electrical equivalent circuits (EECs), while LPR and EN results were processed to determine corrosion current density (i_{corr}), corrosion rates (CR), and inhibition efficiency (IE) using established equations (Anita et al., 2023; Jung and Lee, 2024; Ura-Bińczyk et al., 2021).

2.6. 1D-pit techniques

One-dimensional (1D) artificial pit electrodes were fabricated using welded CS wires with a diameter (1000 μm), including CS-PM, CS-WM, and CS-HAZ variants, embedded in epoxy resin.

A custom-designed mold, created via 3D printing, enabled the assembly of a vertical multi-electrode array to facilitate simultaneous testing of electrodes with and without conductive deposits, specifically SiO_2 and $CaCO_3$ (**Fig. 2a**). The array was immersed in a simulated sour electrolyte to investigate localized pit formation under controlled conditions. The welded CS specimens underwent wet abrasion to a 2000-grit finish to ensure uniform exposure to the electrolyte (**Fig. 2b**). To enhance the accuracy of pit depth measurements and minimize experimental artifacts, vacuum-assisted resin curing was employed to eliminate microbubbles, while thorough cleaning of the wires prevented crevice formation and contamination. These procedural refinements significantly improved the reliability of the experimental setup for studying localized corrosion mechanisms in welded CS structures.

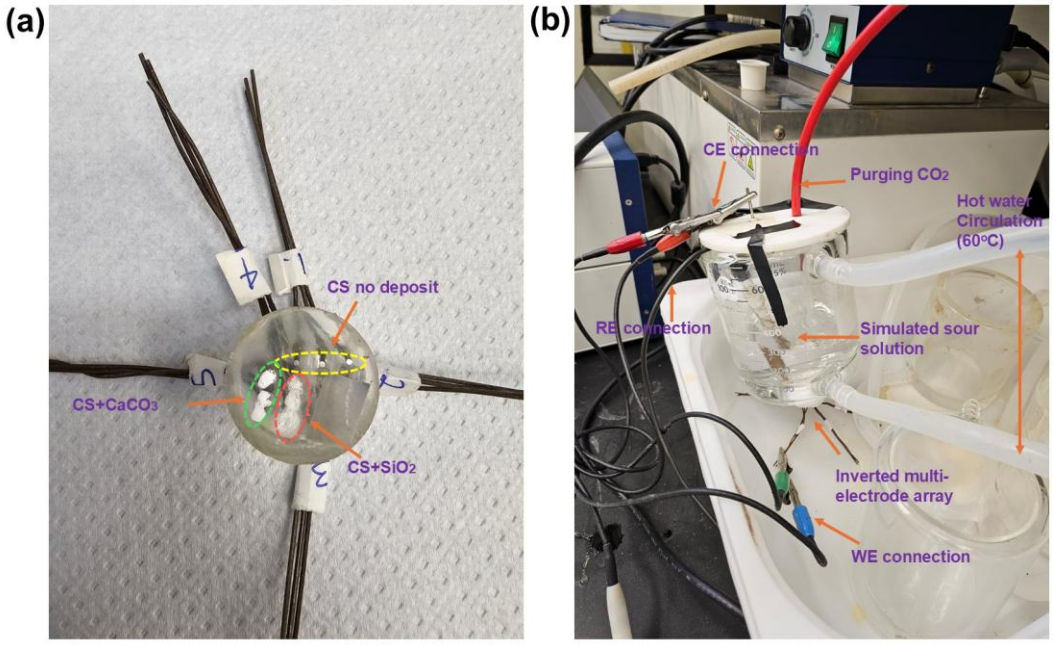

Fig. 2: A setting-up of 1D artificial pit technique (a) a plastic cup fastened at the pit mouth with wires in diameter (1000 µm) embedded in transparent epoxy, without and with SiO_2 or $CaCO_3$ deposits, and (b) vertically inverted 1D multiple electrodes in sour electrolyte connected to the Potentiostat for the creation of an artificial cavity with anodic polarization at +500 mV employing a 3-electrode configuration to recessed the wire within the epoxy.

Pitting conditions are frequently simulated in the laboratory using the 1D artificial pit approach, which uses forced polarization conditions at high positive potential (+500 mV). Given that the experimental settings differed from actual corrosive environments, this provides important controlled mechanistic insights (pit initiation/growth and propagation). In the experimental debate of pitting assessment, this leads to differences between OCP (i.e., real-world corrosion propensity)

and forced polarization (i.e., artificial pit growth or breakdown). To replicate genuine pit dissolving kinetics impacted by polarization, diffusion control, and salt layer development influencing corrosion behavior, several investigations have used 1D artificial pit electrodes (Bonzom and Oltra, 2016; Jun et al., 2020; Pessu et al., 2022). Although its ability to depict intricate pit geometries and environmental variations is constrained.

The deposition process on wire electrodes was conducted using a methodology analogous to that employed for rod electrodes, wherein plastic cups and mesh covers were utilized to encapsulate the wire cross-section. Electrochemical characterization techniques, including potentiostatic, OCP, and EIS, were applied both in the absence/presence of deposits (SiO_2 or $CaCO_3$) over the artificial pit cavity. The experimental setup involved a sour electrolyte solution with the electrodes functioning as anodes at an elevated temperature of 60 °C. This approach facilitated the quantification of critical parameters such as pit depth (d_{pit}), pit area, pit density, aspect ratio, pit resistance (R_{pit}), pit current density (i_{pit}), and pit propagation rates across various welded regions (CS-PM, CS-WM, and CS-HAZ) under simulated sour conditions without/with specific deposits (SiO_2 or $CaCO_3$). The calculation of pit depth was based on Faraday's second law of electrolysis.

2.7. Surface morphology and characterization

The X65 welded CS coupons, representing different regions, i.e., PM, WM, and HAZ, were subjected to comprehensive analysis using advanced characterization techniques. Scanning electron microscopy (SEM) coupled with energy-dispersive X-ray spectroscopy (EDX) was employed to investigate surface morphology, elemental composition, and spatial distribution of elements both before and after corrosion testing. Bulk metal composition was determined through X-ray fluorescence (XRF), while optical microscopy provided insights into the microstructural features of the samples. Raman spectroscopy was utilized to characterize the corrosion products formed on welded coupons under sour conditions, without/with SiO_2 or $CaCO_3$ deposits, and in the absence/presence of CRW11 inhibitors, offering a detailed understanding of the chemical transformations associated with corrosion processes.

2.8. Dataset construction and machine learning model development

The dataset integrates measurements obtained from EIS, LPR, and EN techniques, providing a robust basis for ML model development. It includes critical variables such as the electrochemical method, regions of welded CS samples, deposit types (SiO_2 or $CaCO_3$), and the presence of the corrosion inhibitor CRW11. To ensure compatibility with ML algorithms, categorical variables were transformed using one-hot encoding, which converts nominal data into binary vectors without introducing ordinal relationships. The final dataset comprises 144 data points, evenly distributed across the three electrochemical techniques, ensuring balanced representation for model training and analysis.

The dataset was systematically divided into input features and a single output target (IE). Input features encompassed electrochemical methodologies, deposit types, formation characteristics, CRW11 inhibitor types, and experimental measurements derived from EIS, LPR, and EN techniques. This structured partitioning facilitated the construction and evaluation of predictive models to investigate correlations between diverse input variables and the predicted inhibitor efficiency. Stratified sampling was employed to split the dataset into training (80%) and testing (20%) subsets, ensuring the proportional representation of electrochemical methodologies across both subsets. This approach mitigated sampling bias and preserved the population's inherent distribution, enabling robust performance evaluation and generalizability of the ML model across heterogeneous electrochemical data.

Seven regression algorithms, i.e., linear regression (LR), support vector regression (SVR), k-nearest neighbors (KNN) regression, random forest (RF), decision tree (DT), gradient boosting (GB), and extreme gradient boosting (XGBoost), were employed to predict IE in a dataset comprising mixed variable types. The predictive performance of these models was rigorously evaluated using determination coefficient (R^2), root mean square error (*RMSE*) and mean absolute error (*MAE*) as metrics. To enhance generalization and minimize overfitting, a 4-fold cross-validation strategy was implemented, systematically partitioning the data into training and testing subsets across iterations. This methodological framework facilitated a robust comparative analysis of the algorithms, ensuring a comprehensive assessment of their predictive capabilities across diverse data partitions.

3. Results and discussion

3.1. Corrosion measurements

The experiments described in this section involved the application of controlled preconditioning protocols to welded CS coupons before corrosion testing. These investigations were conducted under simulated sour conditions, incorporating systematic variations in the presence/absence of SiO_2 or $CaCO_3$ deposits, as well as the exclusion/inclusion of the CRW11 corrosion inhibitor.

3.1.1 Open circuit potential

In simulated sour conditions, the E_{OCP} of CS parent metal (CS-PM) and weld metal (CS-WM) was initially lower than that of the heat-affected zone (CS-HAZ). At the onset, CS-PM and CS-WM exhibited cathodic behavior, while CS-HAZ was anodic (**Fig. 3a**). This implies that CS-HAZ is most prone to corrosion in the sour conditions, relative to CS-WM and CS-PM. Over time, the E_{OCP} of CS-WM aligned with that of CS-HAZ, with both transitioning to anodic behavior, whereas CS-PM remained cathodic. Hence, both CS-HAZ and CS-WM are more vulnerable to corrosion. The introduction of the CRW11 inhibitor did not significantly alter these galvanic interactions (**Fig. 3b**). These findings indicate persistent potential differences ($< \pm 150$ mV) among the microstructural regions of welded CS under sour conditions, regardless of inhibitor presence. This behavior is attributed to heterogeneities in microstructure and composition (Park et al., 2021; Yang et al., 2021). The continued existence of these potential differences, even with CRW11, underscores the critical role of welding-induced microstructural variations in influencing electrochemical properties. This highlights the necessity for tailored corrosion mitigation strategies in such complex systems.

The incorporation of SiO_2 deposits before corrosion testing revealed dynamic electrochemical interactions among welded CS components in a simulated sour environment. Initially, CS-PM-SiO_2 exhibited anodic behavior, while CS-WM-SiO_2 and CS-HAZ-SiO_2 acted cathodically. This indicates that CS-PM-SiO_2, amongst the three regions, was more susceptible to corrosion. However, prolonged exposure reversed this configuration, making oxidation of Fe (i.e., more corrosion) in CS-HAZ-SiO_2 and CS-WM-SiO_2 more significant (**Fig. 3c**). The addition of the CRW11 inhibitor further altered the electrochemical dynamics, initially rendering CS-PM-SiO_2-CRW11 and CS-WM-SiO_2-CRW11 cathodic, but CS-HAZ-SiO_2-CRW11 anodic (**Fig. 3d**). Over time, CS-WM-SiO_2-CRW11 and CS-PM-SiO_2-CRW11 transitioned to anodic roles, while

CS-HAZ-SiO_2-CRW11 changed to cathodic. These findings highlight the complex interplay between SiO_2 deposits, welded CS regions, and CRW11 in sour environments, where there was a slight oxidation of Fe in CS-HAZ-SiO_2-CRW11 at the initial immersion but reversed for CS-WM-SiO_2-CRW11 and CS-PM-SiO_2-CRW11 at prolonged exposure. This result suggests potential difference variations in these regions are insufficient to induce galvanic corrosion and offer valuable insights for improving industrial corrosion management strategies.

The deposition of $CaCO_3$ coverage on welded CS specimens, preconditioned for corrosion tests in a simulated sour environment, revealed complex electrochemical interactions. Initially, E_{OCP} analysis showed anodic behavior in CS-PM-$CaCO_3$ and CS-HAZ-$CaCO_3$, while CS-WM-$CaCO_3$ acted as a cathode, but prolonged exposure (24 h) neutralized these differences (**Fig. 3e**). This reveals more oxidation of Fe in both CS-PM-$CaCO_3$ and CS-HAZ-$CaCO_3$ relative to CS-PM-$CaCO_3$. The addition of the CRW11 inhibitor reversed this distribution, making CS-PM-$CaCO_3$-CRW11 and CS-HAZ-$CaCO_3$-CRW11 cathodic and CS-WM-$CaCO_3$-CRW11 anodic (**Fig. 3f**). Over time, a reconfiguration occurred, stabilizing CS-PM-$CaCO_3$-CRW11 and CS-WM-$CaCO_3$-CRW11 as cathodic and transitioning CS-HAZ-$CaCO_3$-CRW11 to anodic. These findings highlight that there is more oxidation of Fe in CS-HAZ-$CaCO_3$-CRW11 after long exposure in the sour media compared to CS-WM-$CaCO_3$-CRW11 and CS-PM-$CaCO_3$-CRW11. This offers insights into the time-dependent electrochemical behavior of varied regions of welded CS and potential strategies for improved corrosion mitigation in sour environments.

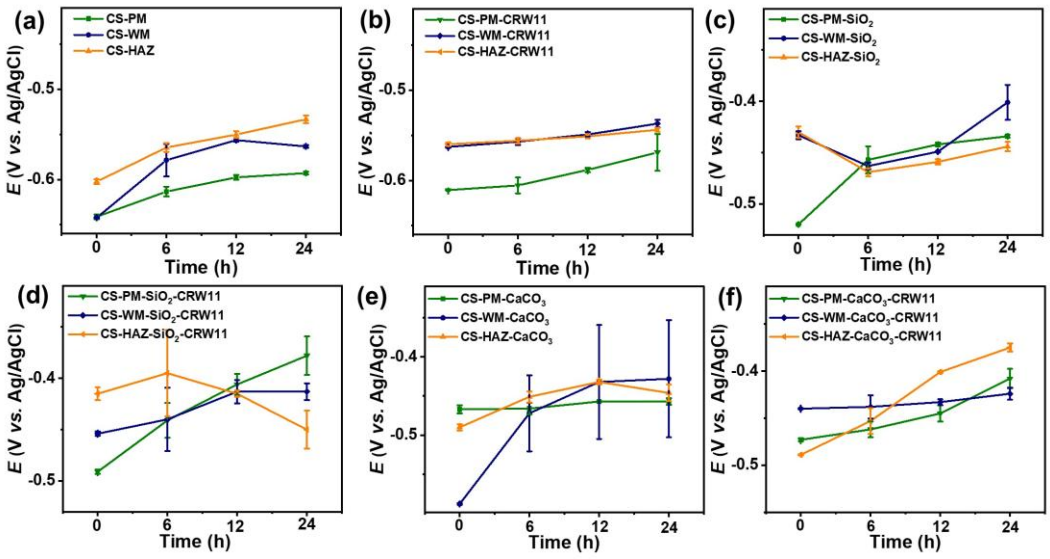

Fig. 3: OCP with preconditioning before corrosion in simulated sour conditions of (a) welded CS, (b) welded CS + CRW11, (c) welded CS + SiO_2, (d) welded CS + SiO_2 + CRW11, (e) welded CS + $CaCO_3$, and (f) welded CS + $CaCO_3$ + CRW11.

3.1.2 Linear polarization potential

The CRs of welded CS specimens were assessed under simulated sour conditions using LPR tests. In the absence of the CRW11 inhibitor, the CRs exhibited a progressive increase over time, with CS-HAZ demonstrating the highest CRs, followed by the CS-WM and CS-PM (**Figs. S1a-c**). The application of the CRW11 inhibitor markedly mitigated corrosion rates, generally reducing them to levels below the industry standard of 0.1 mm/year (**Figs. S1d-f**). However, elevated initial CRs were observed for CS-WM and CS-PM in the presence of CRW11, indicating a delayed onset of optimal inhibitor performance in these regions. This delay may be attributed to microstructural characteristics such as larger and coarser grain boundaries, as suggested in prior studies (Al-Amiery et al., 2023; Kolli et al., 2019; Palumbo et al., 2021). These findings highlight the time-dependent efficacy of CRW11 and emphasize the critical role of microstructural heterogeneity in influencing inhibitor performance in simulated sour environments.

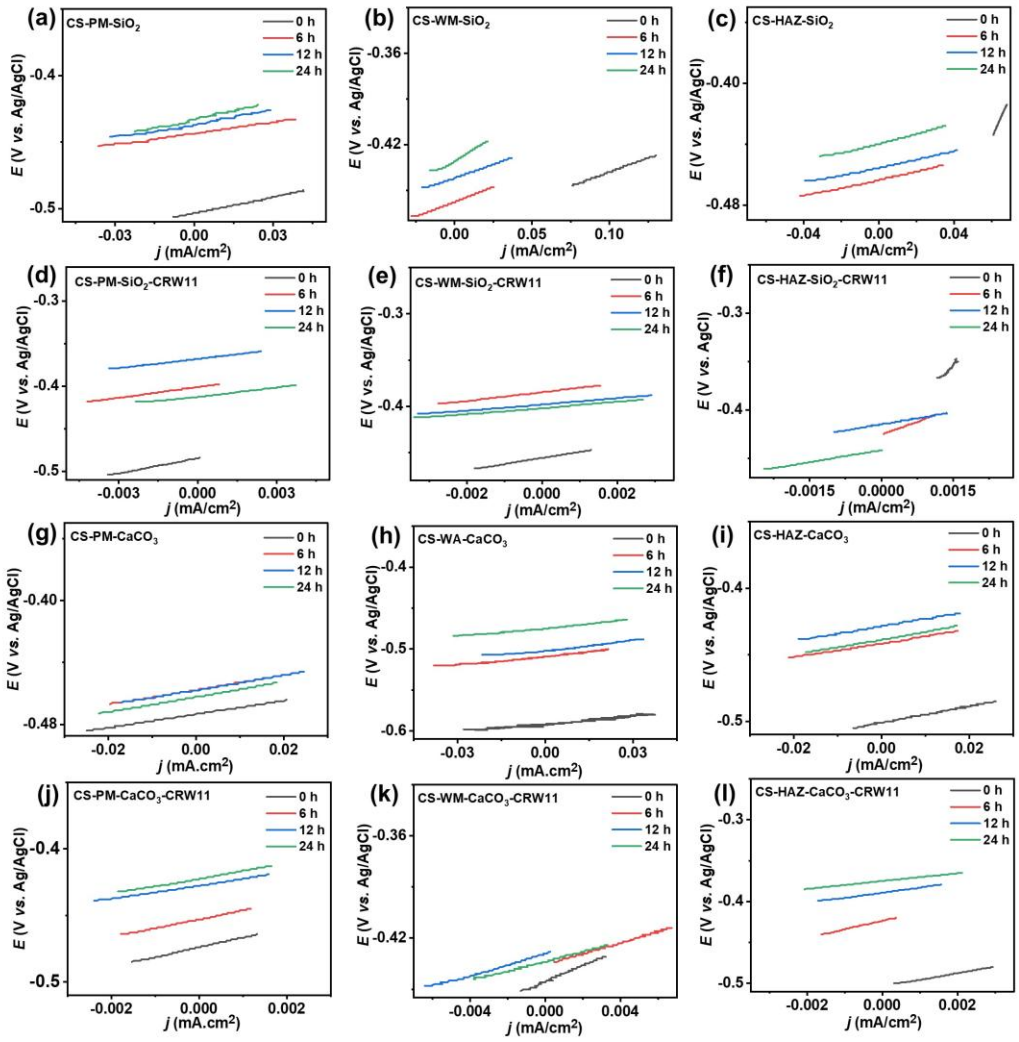

Fig. 4: LPR with preconditioning before corrosion in simulated sour conditions of (a) CS-PM-SiO_2, (b) CS-WM-SiO_2, (c) CS-HAZ-SiO_2, (d) CS-PM-SiO_2-CRW11, (e) CS-WM-SiO_2-CRW11, (f) CS-HAZ-SiO_2-CRW11, (g) CS-PM-$CaCO_3$, (h) CS-WM-$CaCO_3$, (i) CS-HAZ- $CaCO_3$, (j) CS-PM-$CaCO_3$-CRW11, (k) CS-WM-$CaCO_3$-CRW11, and (l) CS-HAZ-$CaCO_3$-CRW11.

A detailed study of corrosion behavior in three welded CS regions with SiO_2 deposit, i.e., CS-HAZ-SiO_2, CS-PM-SiO_2, and CS-WM-SiO_2, under simulated sour conditions. LPR tests revealed that CS-HAZ-SiO_2 was the most corrosion-prone with high CRs (0.93–1.14 mmpy), followed by CS-PM-SiO_2 (0.63–1.01 mmpy) and CS-WM-SiO_2 (0.47–0.81 mmpy) during initial exposure, with temporal fluctuations observed (**Figs. 4a-c**). The addition of the CRW11 inhibitor significantly reduced CRs below the industry threshold of 0.1 mmpy across all regions, maintaining this reduction throughout exposure (**Figs. 4d-f**). CS-HAZ-SiO_2-CRW11 exhibited the lowest CRs (0.01–0.04 mmpy), while CS-WM-SiO_2-CRW11 and CS-BM-SiO_2-CRW11 showed

slightly higher rates (0.05–0.09 mmpy). Enhanced inhibitor efficacy in the heat-affected zone suggests improved surface coverage and reactivity, highlighting CRW11's possibility to mitigate corrosion in welded CS regions for industrial applications in harsh environments.

The assessment of corrosion behavior for three welded CS regions with $CaCO_3$ deposit, i.e., CS-WM-$CaCO_3$, CS-PM-$CaCO_3$, and CS-HAZ-$CaCO_3$, under simulated sour conditions using the LPR technique, with preconditioning and 75% $CaCO_3$ deposit coverage. The CS-WM-$CaCO_3$ region exhibited the highest CRs (0.79–0.93 mmpy), followed by CS-PM-$CaCO_3$ (0.61–0.72 mmpy) and CS-HAZ-$CaCO_3$ (0.52–0.55 mmpy), despite temporal variations (**Figs. 4g-i**). The addition of the CRW11 corrosion inhibitor reduced CRs across all regions to below 0.1 mmpy, meeting industry standards, with sustained performance throughout exposure. CS-HAZ-$CaCO_3$-CRW11 and CS-PM-$CaCO_3$-CRW11 showed similar lower rates (0.04–0.06 mmpy) compared to CS-WM-$CaCO_3$-CRW11 (0.06–0.09 mmpy) (**Figs. 4j-l**). These results highlight CRW11's effectiveness in mitigating corrosion through surface coverage, adsorption, and reactivity, demonstrating its potential as a robust inhibitor for industrial applications in sour environments.

3.1.3 Electrochemical impedance spectroscopy

EIS was employed to assess the CRs on preconditioned test samples (Ipadeola et al., 2022; Ipadeola et al., 2023a; Ipadeola et al., 2023b). Nyquist plots obtained for CS-PM, CS-WM, and CS-HAZ exhibited well-defined semicircular arcs, with some samples displaying diffusion-related features in the low-frequency region (**Figs. S3a-c**). The addition of the CRW11 inhibitor resulted in an increase in the size of these arcs (**Figs. S3d-f**). Voigt-type equivalent electrical circuit (EEC) models (**Figs. S3g, h**) were utilized to analyze the impedance data and extract polarization resistance (R_p), which is inversely proportional to CR. The R_p values followed the trend CS-PM > CS-WM > CS-HAZ, corresponding to increasing CRs: CS-PM < CS-WM < CS-HAZ. Notably, the introduction of CRW11 effectively reduced CRs to below 0.1 mmpy in most cases, which remained within the experimental error margin (Ribeiro et al., 2015). However, a substantial protective film/barrier of CRW11 is initially formed on the CS-HAZ-CRW11 and CS-WM-CRW11 with the lowest CR (or highest R_p) at 0 h. These findings indicate that the application of CRW11 significantly mitigated corrosion without inducing adverse effects on the corrosion rates of the tested samples.

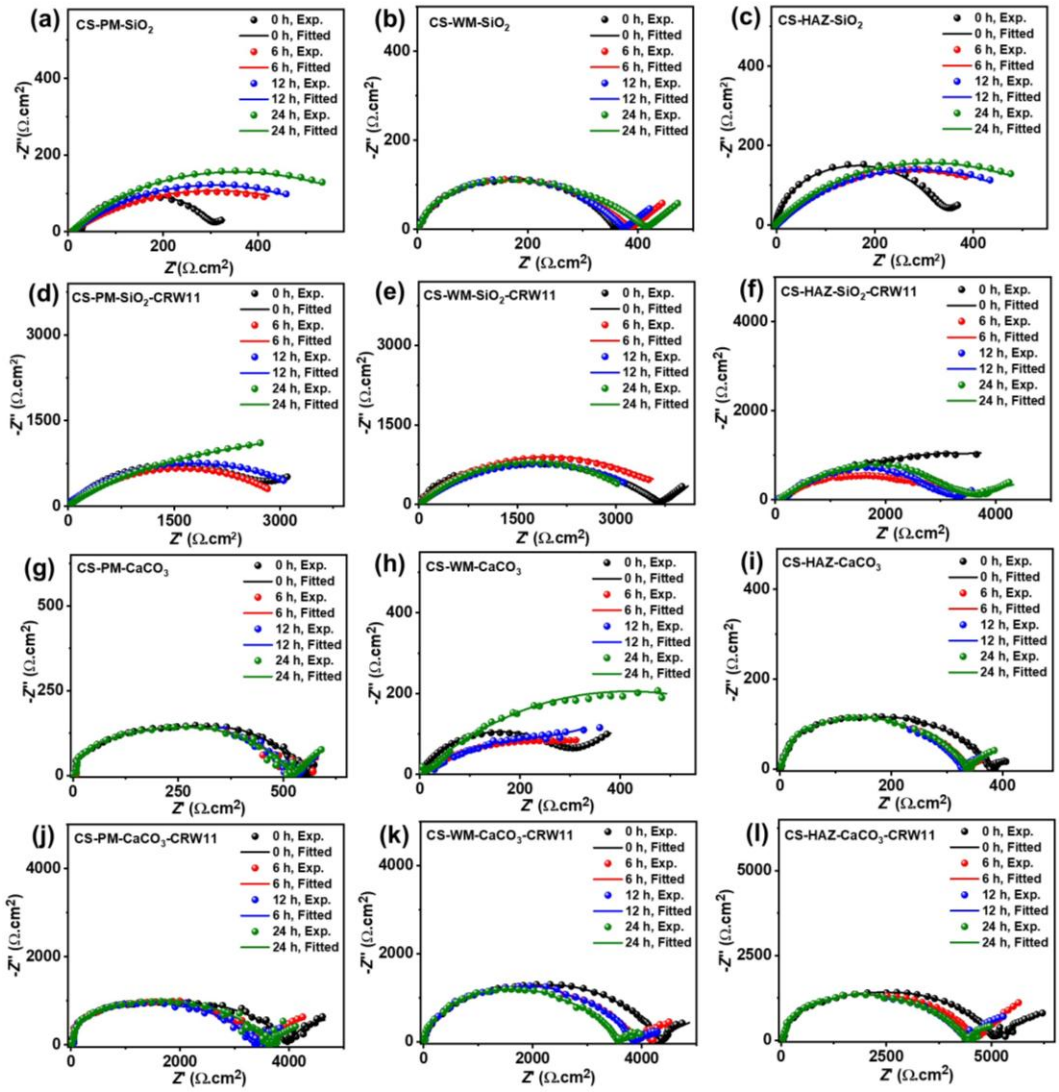

Fig. 5: Nyquist plots with preconditioning before corrosion in simulated sour conditions of (a) CS-PM-SiO_2, (b) CS-WM-SiO_2, (c) CS-HAZ-SiO_2, (d) CS-PM-SiO_2-CRW11, (e) CS-WM-SiO_2-CRW11, (f) CS-HAZ-SiO_2-CRW11, (g) CS-PM-$CaCO_3$, (h) CS-WM-$CaCO_3$, (i) CS-HAZ-$CaCO_3$, (j) CS-PM-$CaCO_3$-CRW11, (k) CS-WM-$CaCO_3$-CRW11, and (l) CS-HAZ-$CaCO_3$-CRW11.

EIS was used to assess the CRs of welded CS samples preconditioned with SiO_2 deposits. Nyquist plots for CS-PM-SiO_2, CS-WM-SiO_2, and CS-HAZ-SiO_2 showed semicircular arcs, with some indicating diffusion-controlled behavior (**Figs. 5a-c**). The addition of the CRW11 inhibitor significantly enhanced these profiles (**Figs. 5d-f**), as reflected in Voigt-type EEC model (**Figs. S3g, h**) analysis. The R_p values increased in the order: CS-WM-SiO_2 < CS-HAZ-SiO_2 < CS-PM-SiO_2, while the CR followed the reverse trend: CS-WM-SiO_2 > CS-HAZ-SiO_2 > CS-PM-SiO_2. Notably,

CRW11 reduced corrosion rates to below 0.1 mmpy for most samples, except for CS-PM-SiO_2-CRW11 at 6 h, which reached the threshold value.

EIS was employed to assess the CRs of preconditioned welded CS samples with $CaCO_3$ deposits. Nyquist plots revealed semicircular arcs, with some samples showing diffusion regions (**Figs. 5g-i**), which expanded significantly upon the addition of the CRW11 inhibitor (**Figs. 5j-l**). Voigt-type EEC models (**Figs. S3g, h**) were used for data analysis, yielding R_p values in descending order: CS-PM-$CaCO_3$ > CS-HAZ-$CaCO_3$ > CS-WM-$CaCO_3$, inversely correlating with CRs. The CR pattern was CS-WM-$CaCO_3$ > CS-HAZ-$CaCO_3$ > CS-PM-$CaCO_3$. The CRW11 inhibitor effectively reduced CRs across all samples to below 0.1 mmpy, demonstrating substantial corrosion mitigation.

3.1.4 Electrochemical noise

EN measurements evaluated the corrosion behavior of welded CS regions (CS-PM, CS-WM, and CS-HAZ) with preconditioning in simulated sour environments. Uninhibited CRs displayed time-dependent fluctuations, ranked as CS-PM (0.58–1.21 mmpy) > CS-HAZ (0.49–0.79 mmpy) > CS-WM (0.51–0.51 mmpy) (**Figs. S2a-c**). This trend contrasts with those measured from LPR and EIS due to variations in measurement techniques, data interpretation, and sensitivity of the EN technique. CRW11 inhibitor application reduced CRs below the 0.1 mmpy industry threshold, stabilizing all regions of welded CS (**Figs. S2d–f**). The results reveal that the CS-PM is most susceptible to corrosion, and the efficacy of the CRW11 inhibitor achieved uniform adsorption, surface coverage, and reactivity across welded zones, ensuring comprehensive protection.

The corrosion resistance of welded CS regions with SiO_2 deposit (i.e., CS-PM-SiO_2, CS-WM-SiO_2, CS-HAZ-SiO_2) under simulated sour conditions was examined via EN after preconditioning. Without the CRW11 inhibitor, CRs varied temporally, peaking in CS-WM-SiO_2 (1.55–2.52 mmpy), followed by CS-HAZ-SiO_2 (1.52–1.64 mmpy) and CS-PM-SiO_2 (0.61–1.23 mmpy) (**Figs. 6a-c**). CRW11 addition suppressed CRs below the 0.1 mmpy threshold in all regions, with inhibited rates ordered as CS-HAZ-SiO_2-CRW11 (0.02 mmpy) < CS-WM-SiO_2-CRW11 (0.02–0.04 mmpy) < CS-PM-SiO_2-CRW11 (0.06–0.08 mmpy) (**Figs. 6d-f**). The inhibitor's efficacy arises from enhanced surface coverage, adsorption, and reactivity on SiO_2-deposited welded zones, ensuring effective protection across all regions.

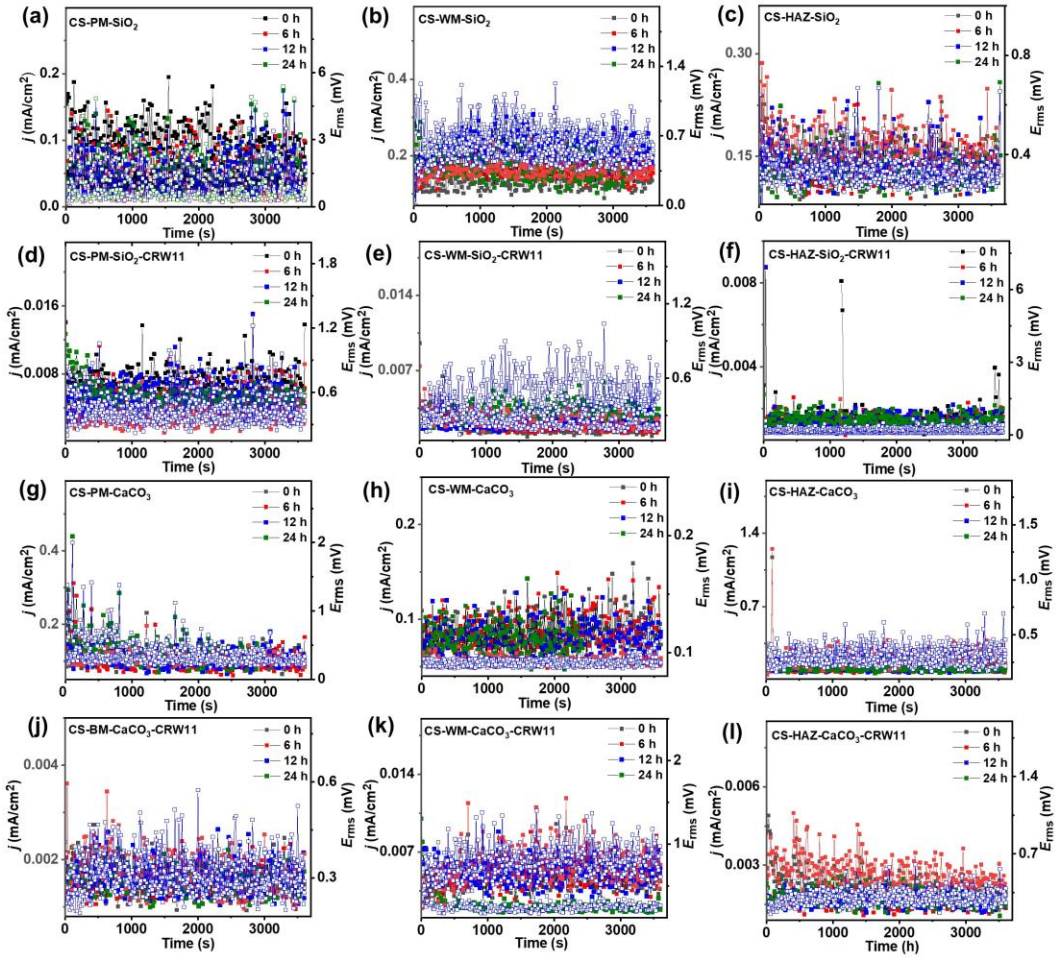

Fig. 6: EN with preconditioning before corrosion in simulated sour conditions of (a) CS-PM-SiO_2, (b) CS-WM-SiO_2, (c) CS-HAZ-SiO_2, (d) CS-PM-SiO_2-CRW11, (e) CS-WM-SiO_2-CRW11, (f) CS-HAZ-SiO_2-CRW11, (g) CS-PM-$CaCO_3$, (h) CS-WM-$CaCO_3$, (i) CS-HAZ- $CaCO_3$, (j) CS-PM-$CaCO_3$-CRW11, (k) CS-WM-$CaCO_3$-CRW11, and (l) CS-HAZ-$CaCO_3$-CRW11.

The corrosion behavior of three preconditioning welded CS regions with $CaCO_3$ deposits, i.e., CS-PM-$CaCO_3$, CS-WM-$CaCO_3$, and CS-HAZ-$CaCO_3$, was systematically studied under simulated sour conditions using EN methodology. Without the CRW11 inhibitor, CRs fluctuated over time, with CS-PM-$CaCO_3$ showing the highest CRs (1.12–1.51 mmpy), followed by CS-HAZ-$CaCO_3$ (1.22–1.42 mmpy) and CS-WM-$CaCO_3$ (0.92–1.02 mmpy) (**Figs. 6g-i**). The addition of CRW11 significantly reduced CRs across all regions, maintaining values below the industry threshold of 0.1 mmpy throughout exposure. Inhibited CRs followed the trend: CS-PM-$CaCO_3$-CRW11 (0.02 mmpy) ≤ CS-HAZ-$CaCO_3$-CRW11 (0.02–0.03 mmpy) < CS-WM-$CaCO_3$-CRW11 (0.03–0.06 mmpy) (**Figs. 6j-l**). These results highlight the base metal's higher corrosion

susceptibility and demonstrate the effectiveness of CRW11 in providing robust protection through superior adsorption, surface coverage, and reactivity on welded regions with $CaCO_3$ deposits.

3.1.5 Comparative electrochemical corrosion rates

A detailed comparative analysis of CRs derived from EIS, LPR, and EN techniques provides critical insights into the corrosion behavior of welded CS samples under varying conditions. Notably, the CS-HAZ consistently exhibited the highest CR values in both EIS and LPR measurements, underscoring its heightened susceptibility to corrosion within welded CS structures (**Fig. 7a**). However, this trend was reversed in EN as CS-PM > CS-HAZ > CS-WM due to variations in (i) measurement techniques, (ii) data interpretation, and (iii) sensitivity, EN data showed an inverted trend in CRs. Notably, EN monitors spontaneous variations in current and potential linked to natural corrosion processes (Jamali and Mills, 2016; Jáquez-Muñoz et al., 2024), in contrast to LPR and EIS. Noise resistance (R_n = potential noise/current noise), which is used to interpret EN data, is not necessarily equivalent to R_p and can be affected by pitting, surface shape, and how noise is statistically treated (Cheng et al., 2019). Also, the recorded signals exhibit noticeable and irregular variations due to EN's heightened sensitivity to localized corrosion events (Jáquez-Muñoz et al., 2024). However, for corrosion testing, LPR and EIS are better than EN because of their higher quantitative accuracy, controlled environments, and mechanistic insights. The CRs determined by LPR and EIS are therefore more consistent and dependable, which supports their application in this study. The application of the CRW11 inhibitor demonstrated significant corrosion mitigation across all regions, achieving IE values exceeding 75%, except at 0 h (**Fig. 7b**). The performance of CRW11 varied by region, with CS-HAZ-CRW11 attaining a peak IE of 81.3% immediately upon exposure, while CS-WM-CRW11 and CS-PM-CRW11 reached their maximum IE values after 12 h of exposure. This observation suggests a gradual adsorption of CRW11 molecules onto the CS-HAZ surface, offering immediate protection against corrosion in the sour electrolyte environment. Comprehensive corrosion data for all regions, obtained through EIS, LPR and EN measurements under simulated sour conditions with and without the CRW11 inhibitor (**Table S1**).

This study shows that the CRW11 inhibitor has a high IE (65.5–92.4%) and decreased CRs for welded CS regions: CS-PM (0.34–0.42 mmpy), CS-WM (0.39–0.73 mmpy), and CS-HAZ (0.48–1.75 mmpy) as assessed by LPR and EIS. Welded CS exposed to *Nephelium lappaceum*

extract: BM (4.1 mmpy), WM (19.3 mmpy), and HAZ (4.0 mmpy) showed IE (31.0-97.0%) (Gapsari et al., 2021); other welded zones: W1 (2.1 mmpy), W2 (1.5 mmpy), and W3 (1.3 mmpy) (Lu et al., 2016); and PM (4.2 mmpy), WM (14.2 mmpy), and HAZ (9.0 mmpy) were inhibited by an imidazoline-based compound (73.0-85.0%) (Nik Mohamed Daud et al., 2023). **Table S2** summarizes the comparison with other reported systems. The corrosion behavior of welded CS samples under various conditions, including preconditioning, SiO_2 deposits, and absence/presence of the CRW11 inhibitor in simulated sour conditions (**Fig. 7c**). Among the regions studied, CS-HAZ-SiO_2 consistently exhibited the highest CR values, indicating greater susceptibility to corrosion in SiO_2-deposited environments. The CRW11 inhibitor demonstrated exceptional efficacy, achieving IE values above 80% across all regions during the exposure period, peaking at 99.6%, 94.0%, and 93.6% for CS-HAZ-SiO_2-CRW11, CS-WM-SiO_2-CRW11, and CS-PM-SiO_2-CRW11 at 0 h (**Fig. 7d**). This suggests a gradual penetration of CRW11 through the SiO_2 layer and enhanced adsorption on the CS surface, particularly in the heat-affected zone. Detailed corrosion data for all regions under simulated sour conditions without/with CRW11 (**Table 1**).

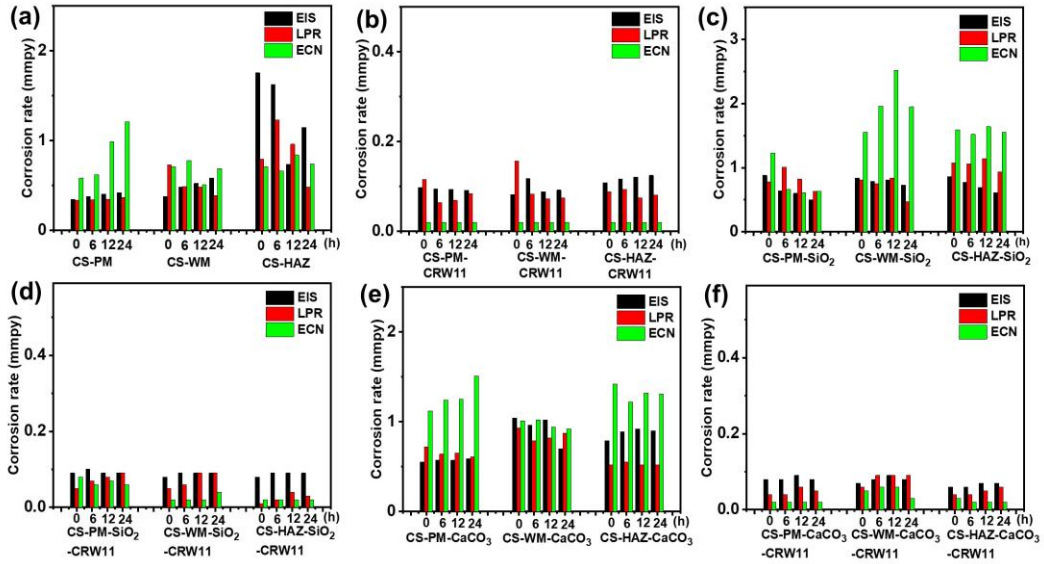

Fig. 7: Comparative CRs with preconditioning before corrosion in simulated sour conditions of (a) welded CS, (b) welded CS + CRW11, (c) welded CS + SiO_2, (d) welded CS + SiO_2 + CRW11, (e) welded CS + $CaCO_3$, and (f) welded CS + $CaCO_3$ + CRW11.

Table 1: Summary of electrochemical results of welded CS samples with preconditioning before corrosion tests, with SiO_2 deposit in absence/presence of CRW11 (200 ppm) in simulated sour electrolyte.

Samples	**Time (h)**	E_{OCP} **(V/Ag/AgCl)**	i_{corr} **(mA/cm²)**	R_{ct} **(Ω.cm²)**	**CR (mmpy)**			**IE (%)**
					EIS	**LPR**	**EN**	
CS-PM-SiO_2	0	-0.520 ± 0.000	0.067 ± 0.013	344 ± 10	0.88 ± 0.18	0.78 ± 0.13	1.23 ± 0.12	-
	6	-0.457 ± 0.013	0.087 ± 0.017	474 ± 20	0.64 ± 0.13	1.01 ± 0.19	0.66 ± 0.11	-
	12	-0.442 ± 0.002	0.071 ± 0.013	504 ± 20	0.60 ± 0.12	0.82 ± 0.16	0.61 ± 0.11	-
	24	-0.434 ± 0.001	0.054 ± 0.011	608 ± 21	0.50 ± 0.15	0.63 ± 0.12	0.63 ± 0.11	-
CS-PM-SiO_2-CRW11	0	-0.491 ± 0.002	0.004 ±0.001	3050 ± 35	0.09 ± 0.02	0.05 ± 0.01	0.08 ± 0.01	93.6
	6	-0.441 ± 0.017	0.006 ±0.001	2921 ± 33	0.10 ± 0.02	0.07 ± 0.01	0.06 ± 0.01	92.9
	12	-0.406 ± 0.010	0.007 ± 0.001	3192 ± 61	0.09 ± 0.02	0.08 ± 0.01	0.07 ± 0.01	90.0
	24	-0.378 ± 0.019	0.008 ± 0.001	3205 ± 99	0.09 ± 0.02	0.09 ± 0.01	0.06 ± 0.01	86.1
CS-WM-SiO_2	0	-0.433 ± 0.004	0.070 ± 0.010	360 ± 46	0.84 ± 0.14	0.81 ± 0.12	1.55 ± 0.31	-
	6	-0.463 ± 0.003	0.065 ± 0.009	385 ± 43	0.79 ± 0.13	0.75 ± 0.11	1.96 ± 0.39	-
	12	-0.449 ± 0.001	0.073 ± 0.011	375 ± 41	0.81 ± 0.14	0.84 ± 0.13	2.52 ± 0.50	-
	24	-0.401 ± 0.017	0.041 ± 0.006	415 ± 53	0.73 ± 0.12	0.47 ± 0.07	1.95 ± 0.39	-
CS-WM-SiO_2-CRW11	0	-0.454 ± 0.002	0.004 ± 0.001	3670 ± 84	0.08 ± 0.01	0.05 ± 0.01	0.02 ± 0.00	94.0
	6	-0.440 ± 0.031	0.006 ± 0.001	3540 ± 11	0.09 ± 0.02	0.06 ± 0.01	0.02 ± 0.00	91.5
	12	-0.413 ± 0.012	0.008 ± 0.001	3190 ± 140	0.09 ± 0.02	0.09 ± 0.01	0.02 ± 0.00	89.4
	24	-0.413 ± 0.008	0.008 ± 0.002	3100 ± 103	0.09 ± 0.02	0.09 ± 0.01	0.04 ± 0.00	81.0
CS-HAZ-SiO_2	0	-0.430 ± 0.005	0.092 ± 0.018	353 ± 13	0.86 ± 0.16	1.07 ± 0.21	1.59 ± 0.33	-
	6	-0.469 ± 0.004	0.092 ± 0.019	394 ± 20	0.77 ± 0.14	1.06 ± 0.21	1.52 ± 0.32	-
	12	-0.459 ± 0.003	0.099 ± 0.021	441 ± 20	0.69 ± 0.12	1.14 ± 0.23	1.64 ± 0.31	-
	24	-0.444 ± 0.005	0.081 ± 0.016	500 ± 24	0.61 ± 0.10	0.93 ± 0.19	1.55 ± 0.31	-
CS-HAZ-SiO_2-CRW11	0	-0.415 ± 0.006	0.004 ± 0.000	3970 ± 75	0.08 ± 0.01	0.01 ± 0.00	0.02 ± 0.00	99.6
	6	-0.395 ± 0.042	0.002 ± 0.000	3315 ± 25	0.09 ± 0.01	0.02 ± 0.00	0.02 ± 0.00	98.3
	12	-0.415 ± 0.003	0.003 ± 0.001	3279 ± 21	0.09 ± 0.01	0.04 ± 0.01	0.02 ± 0.00	96.9
	24	-0.450 ± 0.019	0.003 ± 0.001	3364 ± 21	0.09 ± 0.01	0.03 ± 0.01	0.02 ± 0.00	96.3

The corrosion behavior of welded CS samples under varying conditions, including preconditioning, $CaCO_3$ deposits, and the CRW11 inhibitor. Among the regions studied, CS-WM-$CaCO_3$ consistently exhibited the highest CR values across all exposure intervals, except in the EN method, where this trend reversed (**Fig. 7e**), highlighting the weld metal's heightened susceptibility to corrosion in $CaCO_3$-deposited environments. The CRW11 inhibitor demonstrated exceptional effectiveness (**Fig. 7f**), achieving IE exceeding 85% across all regions, with peak values of 94.1% for CS-PM-$CaCO_3$-CRW11 and 93.5% for CS-WM-$CaCO_3$-CRW11 both at 0 h, and 93.3% for CS-HAZ-$CaCO_3$-CRW11 at 6 h. This indicates rapid penetration of CRW11 through the $CaCO_3$ layer and strong adsorption onto CS surfaces, particularly in WM and PM regions, with a more gradual effect in HAZ. Detailed corrosion data from EIS, LPR, and EN for all regions under simulated sour conditions (**Table S3**).

3.1.6 Raman spectra of the welded carbon steel after corrosion tests

Raman spectroscopy analysis of the different regions of welded CS surfaces, including the CS-PM, CS-HAZ, and CS-WM, immersed in sour media revealed distinct corrosion product compositions in uninhibited samples. Corrosion products on CS-PM and CS-HAZ were predominantly characterized by hematite (α-Fe_2O_3, 410.0 cm^{-1}) (Bleij et al., 2022), lepidocrocite (γ-FeOOH, 527.6 cm^{-1}) (Surnam et al., 2016), magnetite (Fe_3O_4, 635.3 cm^{-1}) (Heuer and Luttge, 2018), and maghemite (γ-Fe_2O_3, 687.0 cm^{-1}) (Surnam et al., 2016). In contrast, CS-WM exhibited a slightly different profile, with hematite (α-Fe_2O_3, 290.9 cm^{-1}) (Bleij et al., 2022), goethite (α-FeOOH, 328.0 cm^{-1}) (Santa et al., 2024; Surnam et al., 2016), along with magnetite, maghemite, and lepidocrocite (**Fig. S4a**). These variations in corrosion products are likely driven by the aggressive sour electrolyte environment, coupled with the microstructural and compositional heterogeneity of the weld metal regions, which promotes localized formation of diverse corrosion product phases.

The addition of the CRW11inhibitor resulted in significant modifications to the Raman spectra of inhibited samples across distinct regions of welded CS, i.e., CS-PM-CRW11, CS-WM-CRW11, and CS-HAZ-CRW11. Each region of CS-PM-CRW11, CS-WM-CRW11, and CS-HAZ-CRW11 exhibited unique sets of low-intensity peaks (**Fig. S4b**), highlighting region-specific interactions between the inhibitor and the corresponding CS surfaces. These spectral differences are closely linked to variations in local microstructure and elemental composition inherent to each

region, where the rapid reaction of CRW11 and CS-HAZ in CS-HAZ-CRW11 facilitates slightly higher intensities for some oxides, leading to improved IE at the HAZ region (Colomban and Slodczyk, 2009). Meanwhile, the intensities were relatively suppressed in CS-WM-CRW11 and CS-PM-CRW11, implying passive coverage of the inhibitor in CS-WM and CS-PM regions. Also, the distinct nature and complexity of corrosion products formed in these areas further contribute to the observed variations in corrosion behavior. A similar observation was previously reported (Li et al., 2025; Natesan et al., 2008). A thorough summary of Raman shifts in all experimental conditions is presented in **Table S4**.

3.2. Morphology and elemental compositions

The elemental compositions of pristine PM, WM, and HAZ were characterized using EDX for surface analysis and XRF for bulk analysis. The pristine PM was predominantly composed of Fe (91.9 wt.%) with trace amounts of alloying elements (**Table S5**). In contrast, the pristine WM exhibited a slightly reduced Fe content (89.9 wt.%) but showed elevated levels of C, Mn and lowered Cr (0.2 wt.%), along with the deliberate addition of Ni (1.0 wt.%) and Zn (1.4 wt.%). The pristine HAZ displayed an intermediate composition between PM and WM. The incorporation of Ni and Zn in the WM was specifically aimed at improving corrosion resistance under sour oil and gas conditions; however, the effectiveness of these additions is contingent upon achieving ideal concentration levels (Fakheri et al., 2020).

XRF analysis was conducted to determine the bulk metal compositions of various regions in pristine welded CS samples. The PM and HAZ exhibited nearly identical metal profiles, primarily composed of Fe (97.8 wt.%) with minor concentrations of Al, Si, Ca, Cr, Mn, Nb, and Mo (**Table S5**). In contrast, the pristine WM displayed a distinct metal composition, characterized by a slightly lower Fe content (97.6 wt.%) and varying levels of Al, Si, Cr, Mn, and Mo, along with the presence of unique elements such as Sc, Ni, and P. Notably, Ca and Nb were detected in the BM and HAZ but were absent in the WM, whereas Sc, Ni, and P were exclusive to the WM region. These compositional variations suggest potential differences in corrosion behavior among the distinct welded regions during subsequent corrosion testing. A large exposed surface area is necessary for XRF to perform effective bulk compositional analysis; however, the corroded CS coupons did not offer enough space for this method. To evaluate the surface elemental compositions of the welded CS coupons following corrosion testing, EDX was utilized.

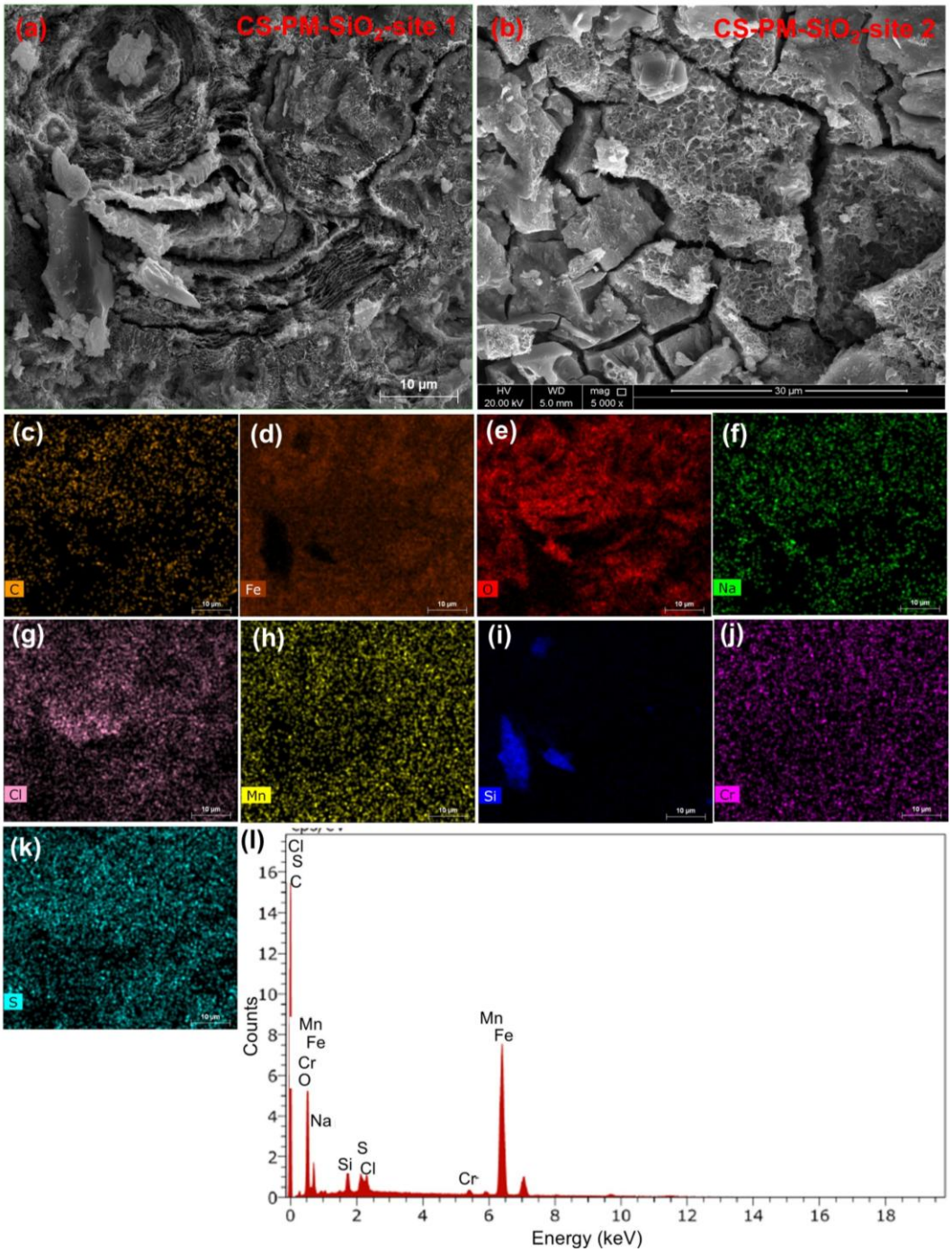

Fig. 8: (a, b) SEM micrographs, elemental mapping of (c) C, (d) Fe, (e) O, (f) Na, (g) Cl, (h) Mn, (i) Si, (j) Cr, and (k) S, and (l) EDX spectra of CS-PM-SiO_2 in simulated sour conditions after corrosion tests.

Following corrosion testing, SEM analysis revealed pronounced surface degradation and the formation of corrosion products across the corroded CS-PM, CS-WM, and CS-HAZ (Katiyar

et al., 2022; Zhang et al., 2022). The original ferritic-pearlite microstructures were largely obscured by the accumulation of corrosion products, as observed (**Figs. S5a, b**, **S6a, b**, **S7a, b**). EDX mapping identified Fe as the predominant element, accompanied by heterogeneous distributions of oxide, sulfide, carbonate, and chloride species across the corroded surfaces (**Figs. S5c-k**, **S6c-k**, **S7c-k**). Both qualitative and quantitative analyses revealed a reduction in Fe content and the presence of corrosion-related elements such as Cl, S, and O on all examined regions (**Figs. S5l**, **S6l**, **S7l**; **Table S6**), indicating accelerated corrosion in the sour electrolyte (Katiyar et al., 2022). Among the analyzed regions, the CS-WM exhibited the highest corrosion rate, as evidenced by elevated concentrations of C, O, and C, followed by the CS-HAZ and then CS-PM. These findings highlight a differential susceptibility to corrosion within welded CS structures, with the weld metal demonstrating the greatest vulnerability.

The incorporation of the CRW11 inhibitor induced mild surface degradation and the formation of corrosion products across all examined regions, as demonstrated by SEM micrographs (**Figs. S8a, b**, **S9a, b**, **S10a, b**). Elemental mapping via EDX revealed iron as the predominant constituent, uniformly distributed alongside other elements (**Figs. S8c-l**, **S9c-l**, **S10c-l**). The inhibitor exhibited notable interaction with the welded CS samples, effectively suppressing the formation of corrosion products in the sour electrolyte environment. This interaction was substantiated by an increased presence of C and Fe, particularly in the CS-HAZ-CRW11 region, accompanied by elevated Na levels (**Figs. S8m**, **S9m**, **S10m**, **Table S6**). Furthermore, the CRW11 inhibitor demonstrated efficacy in mitigating corrosion rates and minimizing the accumulation of corrosion-related elements such as Cl, S, and O, which is consistent with previous reports (Choi and Kim, 2018a; Yang et al., 2021).

SEM analysis of welded CS specimens with SiO_2 deposits (CS-PM-SiO_2, CS-WM-SiO_2, CS-HAZ-SiO_2) revealed pronounced morphological degradation, characterized by extensive surface deterioration and dense accumulation of corrosion byproducts across CS-PM, CS-WM, and CS-HAZ (**Figs. 8a, b**, **9a, b**, **10a, b**). Elemental mapping demonstrated a heterogeneous spatial distribution of constituents, with Fe serving as the predominant constituent, uniformly distributed alongside Mn, Si, and Cr. Localized agglomerations of O, S, C, and Cl compounds were identified through discrete elemental signatures (**Figs. 8c-k**, **9c-k**, **10c-k**), exhibiting variable concentration gradients across microstructural regions. Cl, O, and S exhibited uniform dispersion patterns, as quantified by EDX spectral analysis (**Figs. 8l**, **9l**, **10l**), consistent with atmospheric corrosion

mechanisms involving reduction in O- and S-containing species participation (Yahya et al., 2013). Quantitative elemental analysis revealed Fe contents of 60.2–67.1 wt.% and O contents of 22.4–28.9 wt.% for CS-PM-SiO_2, CS-WM-SiO_2, and CS-HAZ-SiO_2 (**Table S7**). The reduced Fe content compared to welded CS samples without SiO_2 deposits indicates enhanced dissolution under sour conditions in the presence of SiO_2. Elevated S and O levels across all surfaces suggest accelerated corrosion in the sour electrolyte, with CS-WM-SiO_2 and CS-PM-SiO_2 showing higher corrosion rates than CS-HAZ-SiO_2 due to increased O and S concentrations. S and O were identified as the primary corrosion products in CS-WM-SiO_2 and CS-PM-SiO_2, highlighting greater corrosion susceptibility in the CS-WM and CS-PM regions with SiO_2 deposits in a sour environment.

The application of the CRW11 corrosion inhibitor on SiO_2-loaded welded CS substrates led to moderate surface degradation and uniform corrosion product deposition across CS-PM, CS-WM, and CS-HAZ regions, as revealed by SEM and EDX analyses (**Figs. S11a, b**, **S12a, b**, **S13a, b**). Fe was the predominant element (54.1–61.5 wt.%), with heterogeneous distributions of Mn, Si, and Cr, while P, O, S, and Cl mapping indicated reduced inhibitor effectiveness due to SiO_2 deposits (**Figs. S11c-m**, **S12c-m**, **S13c-m**). However, CRW11 effectively limited subsurface propagation of corrosive species. Quantitative analysis showed region-specific elemental variations, including elevated Na, P, S, and C in CS-PM-SiO_2; higher O and Cl in CS-WM-SiO_2; and superior Si retention with minimal S in CS-HAZ-SiO_2 (**Table S7**). Enhanced Fe and O concentrations in CS-WM-SiO_2 samples suggested improved interfacial interactions between CRW11 and the CS matrix, reducing chloride and sulfur accumulation compared to controls. This indicates that CRW11 stabilizes the Fe oxide layer and suppresses SiO_2-mediated oxidation pathways, mitigating corrosion kinetics in sour environment.

SEM analysis revealed extensive surface degradation and corrosion product formation on $CaCO_3$-deposited welded CS samples across the CS-PM-$CaCO_3$, CS-WM-$CaCO_3$, and CS-HAZ-$CaCO_3$ regions (**Figs. S14a, b**, **S15a, b**, **S16a, b**). EDX mapping identified Fe as the dominant element, accompanied by Mn, Si, Ca, and Cr, with uniform distributions of O, S, C, and Cl corrosion products across all regions (**Figs. S14c-m**, **S15c-m**, **S16c-m**). Quantitative data indicated reduced Fe content in CS-PM and CS-HAZ compared to non-deposited samples, highlighting enhanced Fe dissolution under sour conditions (**Table S8**). Elevated concentrations of S and O in CS-PM-$CaCO_3$ and CS-HAZ-$CaCO_3$ samples suggest intensified corrosion processes, with sulfides and oxides as predominant products. These findings underscore differential corrosion

susceptibility within the welded CS structure, with $CaCO_3$-deposited CS-HAZ and CS-PM exhibiting the highest vulnerability to sour environments (Chan, 2003).

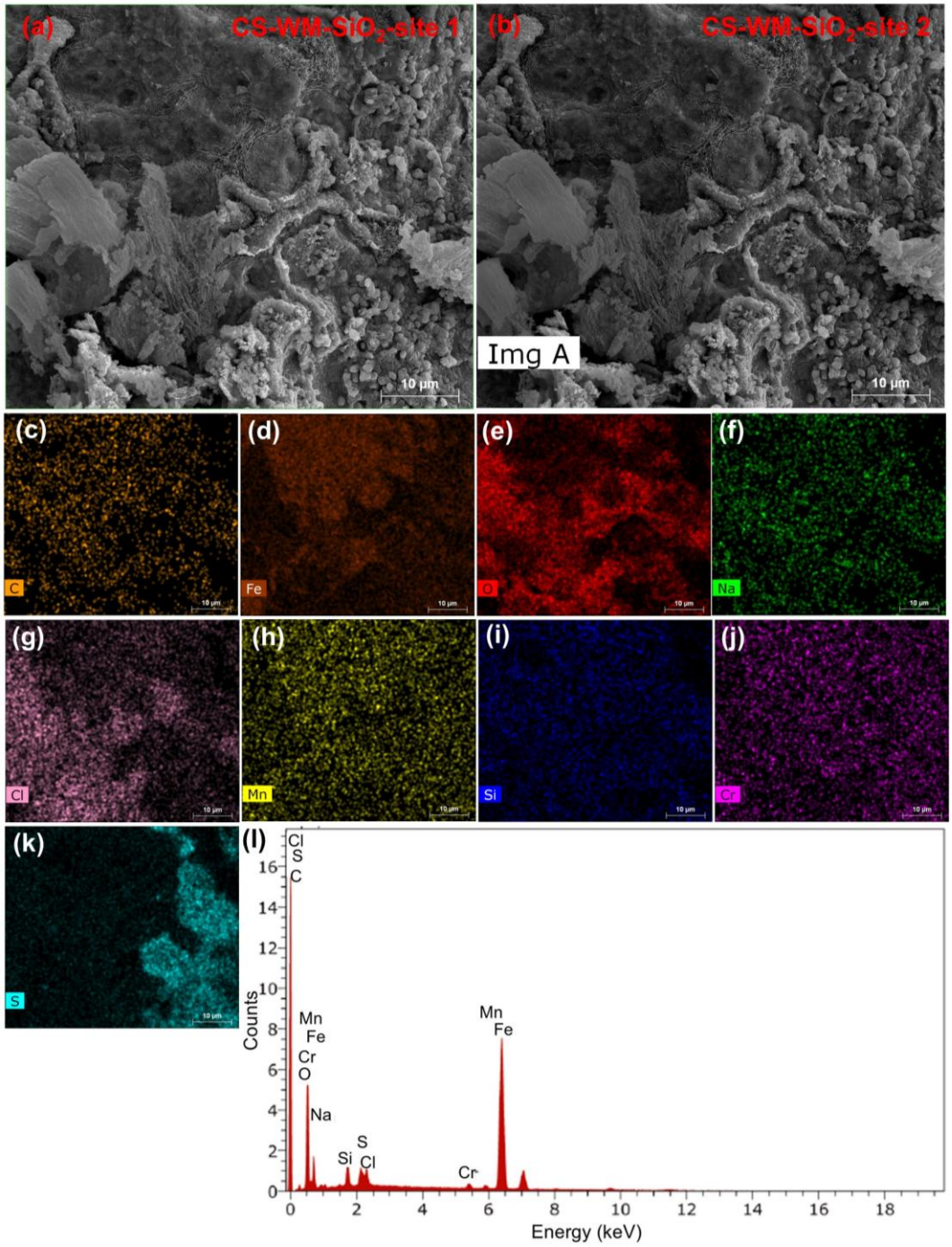

Fig. 9: (a, b) SEM micrographs, elemental mapping of (c) C, (d) Fe, (e) O, (f) Na, (g) Cl, (h) Mn, (i) Si, (j) Cr, and (k) S, and (l) EDX spectra of CS-WM-SiO_2 in simulated sour conditions after corrosion tests.

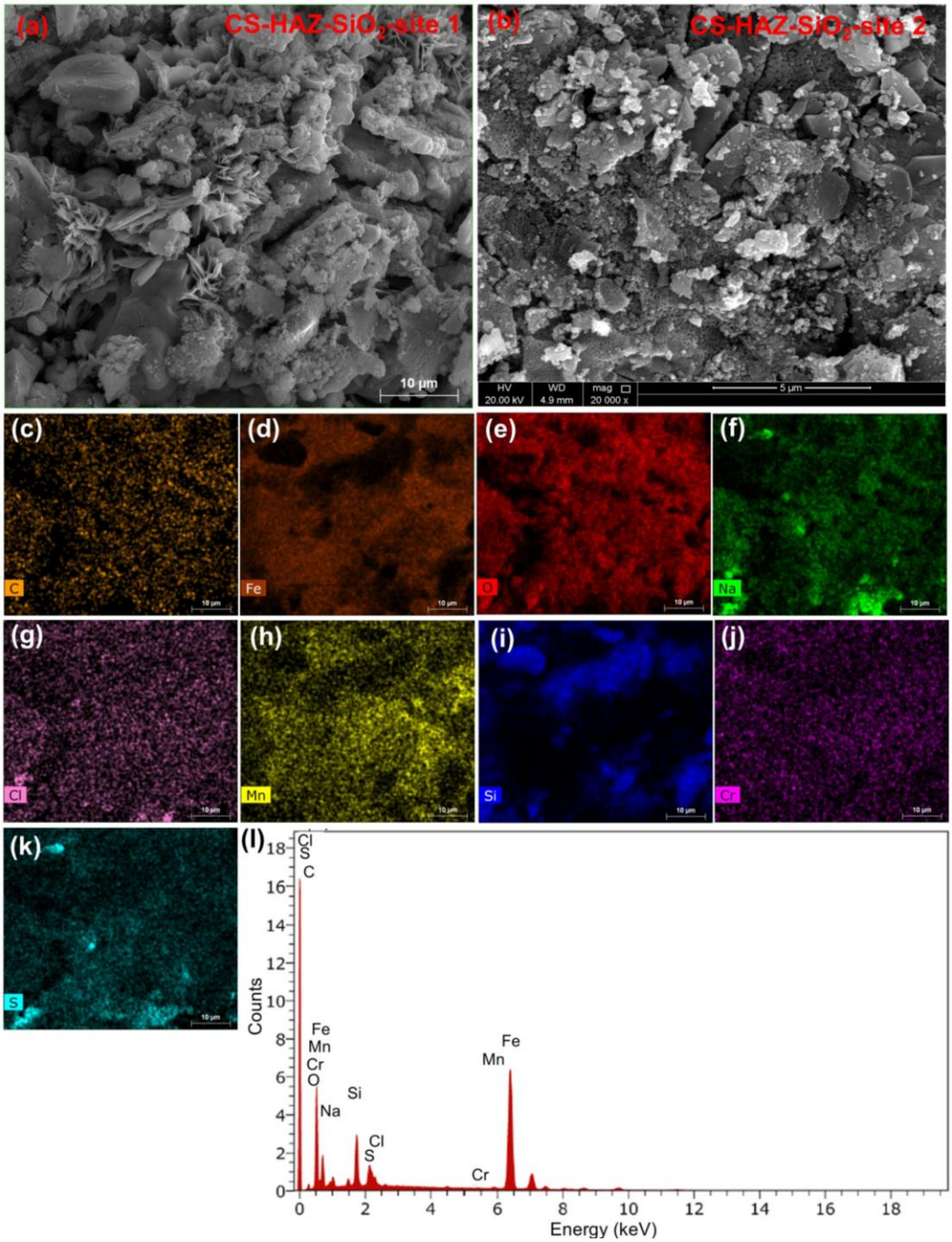

Fig. 10: (a, b) SEM micrographs, elemental mapping of (c) C, (d) Fe, (e) O, (f) Na, (g) Cl, (h) Mn, (i) Si, (j) Cr, and (k) S, and (l) EDX spectra of CS-HAZ-SiO_2 in simulated sour conditions after corrosion tests.

The performance of the CRW11 corrosion inhibitor on $CaCO_3$-loaded welded CS substrates using SEM and EDX analyses. SEM revealed moderate surface degradation and uniform corrosion product deposition across CS-PM-$CaCO_3$, CS-WM-$CaCO_3$, and CS-HAZ-$CaCO_3$ regions (**Figs.**

S17a, b, **S18a, b**, **S19a, b**). EDX spectroscopy identified Fe as the predominant element (54.1 – 61.5 wt.%) with uneven distribution of Mn, Si, and Cr (**Figs. S17c-m**, **S18c-m**, **S19c-m**). The spatial mapping of P, O, S, and Cl indicated reduced CRW11 efficacy due to $CaCO_3$ deposits but confirmed its ability to limit subsurface penetration of corrosive species.

Elemental analysis showed region-specific variations, with CS-HAZ-$CaCO_3$-CRW11 exhibiting higher Na (3.8 wt.%), O (26.6 wt.%), P (0.3 wt.%), S (0.8 wt.%), and C (3.3 wt.%) levels, while CS-WM-$CaCO_3$-CRW11 and CS-BM-$CaCO_3$-CRW11 had increased Fe concentrations (21.1–22.6 wt.%) (**Table S8**). Elevated Fe and O levels in welded regions suggested strong interfacial interactions between CRW11 and the CS matrix, reducing chloride (0.1 wt.%) and sulfur (0.4–0.8 wt.%) accumulation compared to uninhibited controls. These findings demonstrate that CRW11 stabilizes Fe oxide layers and mitigates corrosion by suppressing $CaCO_3$-mediated oxidation pathways in sour environments.

3.3. Microstructure of welded carbon steel

The microstructural evaluation of welded CS coupons revealed distinct phase distributions across PM, WM, and HAZ, driven by localized thermal gradients and welding-induced diffusional kinetics. Optical microscopy (OM) showed the PM to consist of a ferrite-pearlite matrix with elongated grains, indicative of partial recrystallization during prior thermo-mechanical processing (**Fig. S20a**). Better corrosion resistance is demonstrated by the BM with a ferrite-pearlite matrix relative to HAZ and WM because of its more refined microstructure and its ability to form passive protective layers (Zhang et al., 2017). In contrast, WM exhibited a δ-ferrite-dominated microstructure characterized by cellular and columnar dendritic solidification patterns, along with martensite-austenite (M-A) constituents and intragranular acicular ferrite. The absence of pearlite or microcracks in the WM suggests rapid cooling rates that suppress equilibrium phase formation (**Fig. S20b**). Due to WM's high hardness, high internal stresses, and high density of lattice cracks, its martensitic phase is especially susceptible to corrosion in sour media (Orhorhoro et al., 2022; Song et al., 2022). Meanwhile, the HAZ displayed a complex microstructure comprising bainitic transformation products, sparse M-A phases, and fine-grained ferritic regions, without pearlite or stress-induced cracking observed (**Fig. S20c**). The granular bainite presence in the HAZ reduces corrosion resistance due of its coarse microstructure and insufficient passivation properties (Zhang et al., 2017). These microstructural variations highlight the influence of welding thermal cycles,

which promote the development of metastable phases over equilibrium microconstituents due to dynamic thermal and diffusional conditions.

The microstructural analysis of corroded welded CS samples revealed significant corrosion-induced transformations, both in the absence and presence of the CRW11 inhibitor. OM images identified extensive grain boundary attacks and the formation of corrosion products. In the corroded CS-PM (**Fig. S20d**), grain boundary attack was largely concealed by the deposition of corrosion products (Ko et al., 2019). In contrast, the corroded CS-WM (**Fig. S20f**) and CS-HAZ (**Fig. S20h**) exhibited pronounced grain boundary degradation, leading to structural weakening and intergranular separation. This highlights the preferential corrosion of weldments due to their distinct microstructural composition and susceptibility to corrosive environments (Dong et al., 2023). The CS-HAZ was particularly prone to damage, attributed to its fine-grained structure with a higher grain boundary area, which exacerbates vulnerability under corrosive conditions (Choi and Kim, 2018b). However, the application of the CRW11 inhibitor significantly reduced grain boundary attack and corrosion product deposition by forming a hydrophobic protective barrier and scavenging oxygen (Al-Amiery et al., 2023; Chen et al., 2022; Liu et al., 2025). This protective mechanism effectively preserved the original microstructural features across all regions (CS-PM-CRW11, CS-WM-CRW11, and CS-HAZ-CRW11; **Figs. S20e, g, i**), demonstrating the inhibitor's remarkable efficacy in maintaining microstructural integrity under aggressive corrosive environments.

The presence of SiO_2 in three distinct regions of the welded samples, i.e., CS-PM-SiO_2, CS-WM-SiO_2, and CS-HAZ-SiO_2, induces notable microstructural transformations that significantly influence localized corrosion behavior (Xiong et al., 2020). OM analysis reveals SiO_2-mediated alterations in grain boundary morphology within CS-PM-SiO_2, leading to grain boundary failure (**Fig. 11a**). In contrast, SiO_2 precipitates in CS-WM-SiO_2 and CS-HAZ-SiO_2 preferentially accumulate along grain boundaries (**Figs. 11c, e**), increasing the interfacial contact area with ferrite grains and compromising grain boundary integrity. This phenomenon establishes electrochemical potential gradients between SiO_2-covered regions and adjacent uncovered areas, thereby promoting localized corrosion (Han, 2009), with the most substantial effects observed in CS-WM-SiO_2 due to defects and the uneven deposition of SiO_2 (Xijing and Yong, 2023). The introduction of the CRW11 inhibitor into the sour electrolyte facilitates the formation of a protective film at the SiO_2-CS interface within the welded samples (**Figs. 11b, d, f**), effectively

reducing both anodic and cathodic current densities while elevating the activation energy for corrosion. Consequently, this protective layer mitigates corrosion kinetics and enhances the overall resistance to localized corrosion.

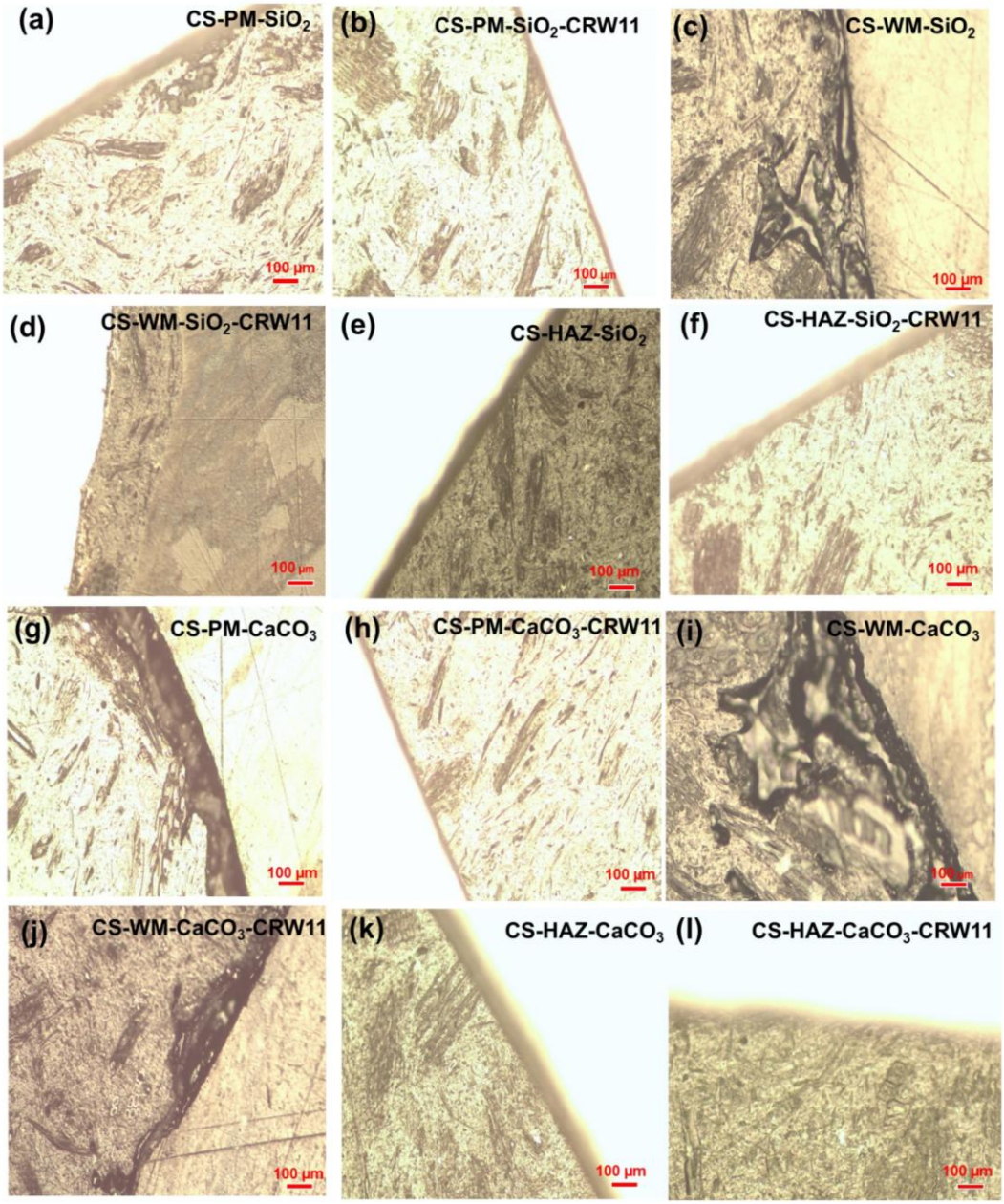

Fig. 11: Microstructure images of (a) CS-PM-SiO_2, (b) CS-PM-SiO_2-CRW11, (c) CS-WM-SiO_2, (d) CS-WM-SiO_2-CRW11, (e) CS-HAZ-SiO_2, (f) CS-HAZ-SiO_2-CRW11, (g) CS-PM-$CaCO_3$, (h) CS-PM-$CaCO_3$-CRW11, (i) CS-WM-$CaCO_3$, (j) CS-WM-$CaCO_3$-CRW11, (k) CS-HAZ-$CaCO_3$, and (l) CS-HAZ-$CaCO_3$-CRW11 after corrosion tests.

The OM analysis demonstrates that $CaCO_3$ incorporation within the microstructural zones of welded CS samples, i.e., CS-PM-$CaCO_3$, CS-WM-$CaCO_3$, and CS-HAZ-$CaCO_3$, induces notable microstructural changes, affecting localized corrosion susceptibility. In CS-PM-$CaCO_3$ and CS-WM-$CaCO_3$, $CaCO_3$ preferentially nucleates at grain boundaries (**Figs. 11g, i**), increasing interfacial contact with the ferrite matrix and causing grain boundary embrittlement, which promotes interfacial decohesion (Weber et al., 2023). Conversely, CS-HAZ-$CaCO_3$ exhibits $CaCO_3$-driven grain boundary reorganization (**Fig. 11k**), altering boundary morphology (Rizzo et al., 2020). Electrochemical heterogeneity arises due to potential differences between $CaCO_3$-deposited regions and exposed CS substrates, forming localized galvanic cells that accelerate corrosion initiation. This effect is more pronounced in CS-PM-$CaCO_3$ and CS-WM-$CaCO_3$ owing to their higher defect density and uneven $CaCO_3$ distribution compared to CS-HAZ-$CaCO_3$. The addition of the CRW11 corrosion inhibitor in sour environments promotes the formation of a chemisorbed protective layer at $CaCO_3$-CS interfaces (**Figs. 11h, j, l**), reducing anodic dissolution and cathodic reduction rates. The inhibitor increases the activation energy for corrosion, significantly lowering corrosion current density and mitigating overall corrosion progression.

3.4. 1D artificial pit technique

The pitting corrosion kinetics of welded CS wires were investigated using a 1D artificial pit technique for controlled pit growth analysis. Electrodes (1 mm diameter) from three welded regions, i.e., CS-PM, CS-WM, and CS-HAZ, were tested without/with SiO_2 or $CaCO_3$ deposits under simulated sour conditions. Potentiostatic testing (at +500 mV vs. Ag/AgCl) for 1 h) showed consistent pit growth across all regions (**Figs. 12a-c**), regardless of deposits, with no significant differences in pit initiation or growth, indicating uniform susceptibility to pitting corrosion.

The pitting corrosion kinetics of 1D welded CS wires, without/with deposits (SiO_2 and $CaCO_3$), were investigated using OCP and EIS. OCP analysis revealed slight variations in the pitting corrosion potential of the CS-PM, with SiO_2 inducing the most anodic shift, and then $CaCO_3$ (**Figs. 12d-f**). The CS-WM exhibited more positive anodic OCP values, identifying it as the most anodic region under sour conditions, regardless of the presence SiO_2 or $CaCO_3$ deposits. Conversely, the CS-HAZ demonstrated anodic behavior like CS-PM, with $CaCO_3$ causing the highest anodicity in CS-HAZ. Overall, CS-WM showed anodic tendencies, while CS-PM and CS-HAZ were cathodic. This implies more Fe oxidation at CS-WM amongst the three regions of

welded CS. However, the potential differences across these regions remained below 150 mV, insufficient to trigger significant galvanic coupling in sour electrolytes.

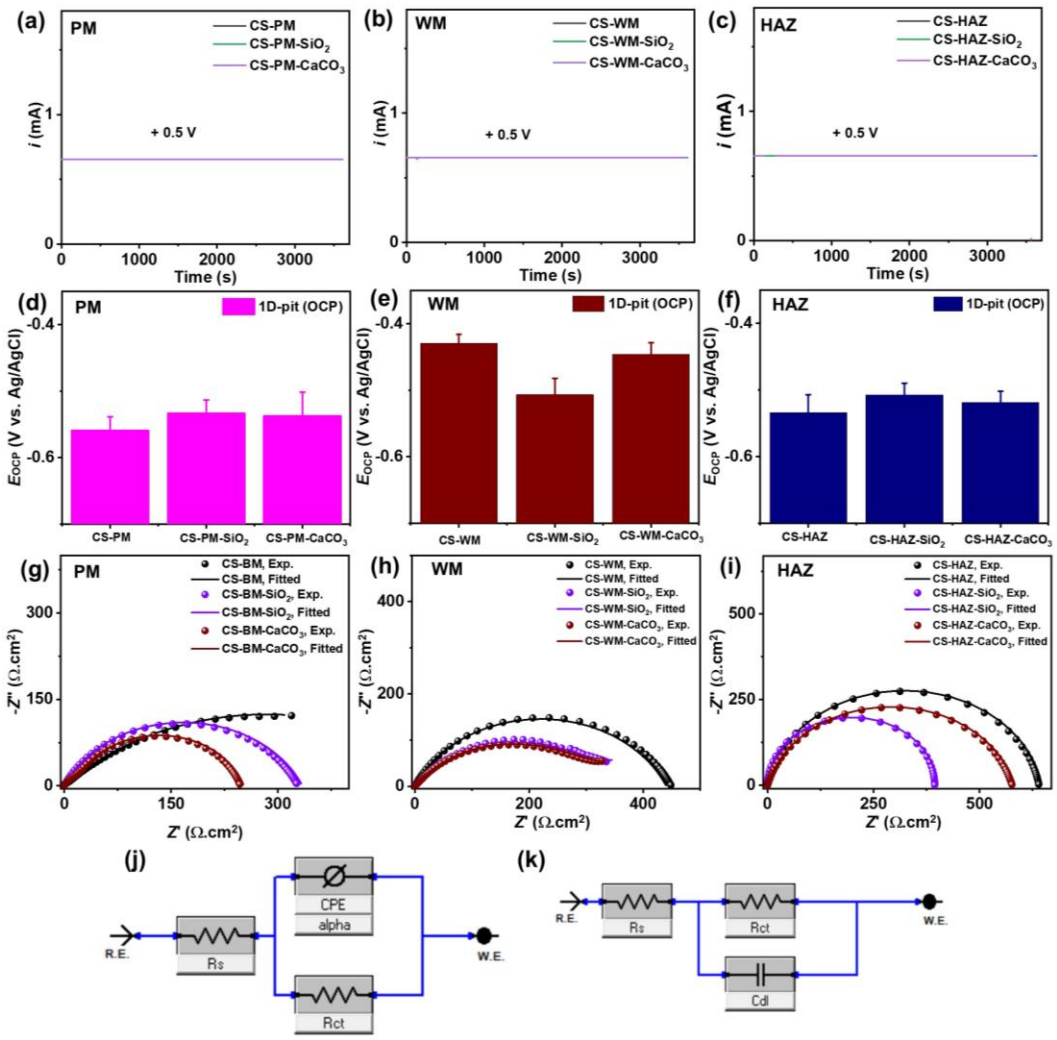

Fig. 12: (a-c) Potentiostatic at +500 mV, (d-f) OCP for 100 s, (g-i) Nyquist plots, and (j, k) Voigt EEC models of welded CS wires (1 mm) with/without deposits (SiO_2 and $CaCO_3$) for 1D-artificial pit growth and propagation in simulated sour conditions.

The pitting polarization resistance (R_{pit}) was quantified via EIS analysis. Nyquist plots for CS-PM, CS-WM, and CS-HAZ, without/with SiO_2 or $CaCO_3$ deposits in sour electrolyte, exhibited semi-circular arcs (**Figs. 12g-i**). EIS parameters were extracted using Voigt EEC models (**Figs. 12j, k**). For the parent metal, R_{pit} decreased in the following order: CS-PM > CS-PM-SiO_2 > CS-PM-$CaCO_3$. This corresponded to increasing pit current densities (i_{pit}) and pit propagation rates in the inverse order. The $CaCO_3$ deposit induced the highest pit propagation rate (1.22 mmpy) on the parent metal. Utilizing Faraday's second law, calculated pit depths (d_{pit}) were derived from

i_{pit} values, yielding mean d_{pit} values of 29.7 ± 0.6, 51.5 ± 1.0, and 68.3 ± 2.7 µm for CS-PM, CS-PM-SiO_2, and CS-PM-$CaCO_3$, respectively. A summary of electrochemical pit kinetics is given in **Table S9**.

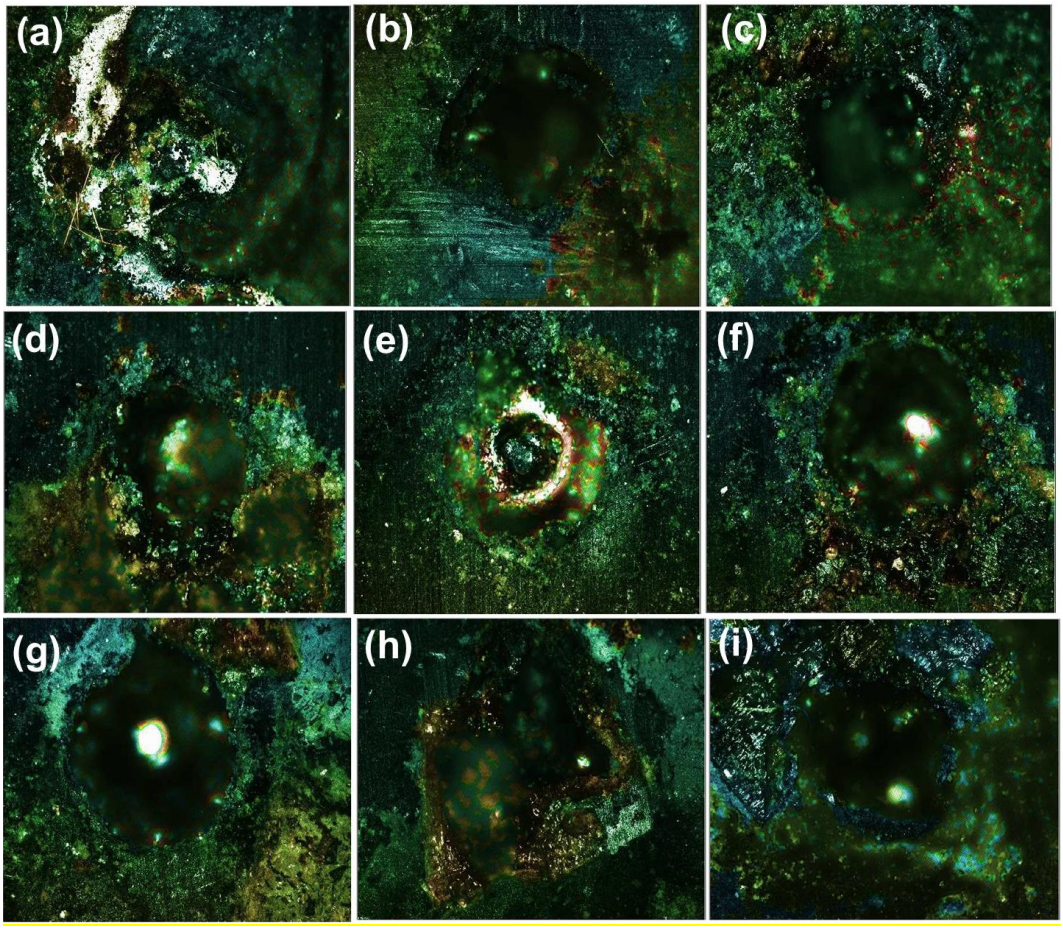

Fig. 13: Optical microscope images of (a-c) CS-HAZ (d-f) CS-HAZ-SiO_2, and (g-i) CS-HAZ-$CaCO_3$ after 1D-artificial pit tests in sour conditions.

For CS-PM without/with SiO_2 or $CaCO_3$ deposits, the actual d_{pit} form OM images ranged from 34.9 ± 7.9 to 53.9 ± 3.8 µm, with aspect ratios spanning 1.9 ± 0.3 to 3.0 ± 0.8, pit areas between 0.008 and 0.009 mm², and pit densities of 122.0 to 123.0 mm^{-2} (**Figs. S21a-i**, **Table 2**). Notably, CS-PM-SiO_2 exhibited the greatest pit depth, while CS-PM-$CaCO_3$ had the largest pit area, and CS-PM showed the highest aspect ratio and pit density.

For the CS-WM without/with SiO_2 or $CaCO_3$ deposit variants, the observed pit depths from OM images ranged from 40.8 ± 4.2 µm to 48.7 ± 7.7 µm, aspect ratios varying between 1.9 ± 0.5 and 2.6 ± 0.3 (**Fig. S22**; **Table 2**). The pit areas were measured between 0.006 mm² and 0.009 mm², while pit densities spanned from 113.2 mm^{-2} to 176.6 mm^{-2}. Among the variants, CS-WM-

$CaCO_3$ exhibited the greatest pit depth and area, whereas CS-WM-SiO_2 demonstrated the highest pit density. The unmodified CS-WM system showed the largest aspect ratio, highlighting distinct morphological characteristics across the different deposit types.

Pitting corrosion characteristics of CS-HAZ without/with SiO_2 or $CaCO_3$ deposits were quantitatively analyzed, revealing d_{pit} ranging from 23.2 ± 0.7 to 44.5 ± 2.3 μm, aspect ratios between 2.4 ± 0.9 and 4.5 ± 0.4, pit areas from 0.007 to 0.008 mm^2, and pit densities from 119.8 to 154.0 mm^{-2} (**Fig. 13**; **Table 2**). Among the variants, CS-PM-SiO_2 exhibited the greatest pit depth, CS-HAZ showed the highest aspect ratio, CS-WM and CS-WM-$CaCO_3$ displayed increased pit area, while CS-WM-Si_2 had the highest pit density. These findings provide a detailed characterization of pitting behavior across welded CS samples and highlight the impact of deposit types on pit morphology and distribution.

Table 2: Parameters obtained from optical microscopes after 1D-artificial pit technique of welded CS wires without/with SiO_2 or $CaCO_3$ deposits in simulated sour conditions

Samples	Actual d_m (μm)	Aspect ratio	Pit area (mm^2)	Pit density (mm^{-2})
Parent metal				
CS-PM	34.9 ± 7.9	3.0 ± 0.8	0.008	123.0
CS-PM-SiO_2	53.9 ± 3.8	1.9 ± 0.3	0.008	122.0
CS-PM-$CaCO_3$	36.9 ± 6.3	2.9 ± 0.6	0.008	120.6
Welding metal				
CS-WM	40.8 ± 4.2	2.6 ± 0.3	0.009	116.7
CS-WM-SiO_2	42.5 ± 16.5	1.9 ± 0.5	0.006	176.6
CS-WM-$CaCO_3$	48.7 ± 7.7	2.2 ± 0.3	0.009	113.2
Heat affected zone				
CS-HAZ	23.2 ± 0.7	4.5 ± 0.4	0.008	119.8
CS-HAZ-SiO_2	41.8 ± 0.9	2.4 ± 0.9	0.007	154.1
CS-HAZ-$CaCO_3$	44.5 ± 2.3	2.6 ± 1.1	0.008	132.8

3.5. Applicability of machine learning algorithms

This investigation employed an ML-driven computational framework to systematically predict localized corrosion dynamics in welded CS samples without/with SiO_2 or $CaCO_3$ deposits exposed to simulated sour environments (Ipadeola et al., 2025). The model integrated multifaceted experimental variables, including distinct welded microstructural zones (i.e., CS-PM, CS-WM, and CS-HAZ), inorganic deposits (SiO_2 or $CaCO_3$), the presence of a corrosion inhibitor

(CRW11), and sour service parameters. A comprehensive dataset of 144 data points was assembled from combined LPR, EN, and EIS analyses, thereby overcoming limitations of prior studies restricted to singular electrochemical techniques (Butler et al., 2018; Coelho et al., 2022; Diao et al., 2021). Categorical features, like welding regions, deposit phases, and inhibitor status, were computationally encoded using one-hot vectors, with IE serving as the regression target. The dataset underwent stratified partitioning into training (70%) and testing (30%) subsets to preserve proportional representation of electrochemical methodologies. Seven regression algorithms (LR, SVR, KNN, RF, DT, GB, and XGBoost) were rigorously assessed through performance metrics (coefficient of determination (R^2), root mean squared error (*RMSE*), mean absolute error (MAE)). This multimodal data fusion strategy, encompassing both electrochemical techniques and heterogeneous environmental variables, constitutes a notable advancement in corrosion prediction accuracy and generalizability under complex service conditions (Chen and Guestrin, 2016).

The cumulative corrosion behavior of welded CS samples, comprising the CS-PM, CS-WM, and CS-HAZ, was systematically investigated under sour environments in the absence/presence of the CRW11 inhibitor (**Fig. 14a**). ML algorithms were employed to model the corrosion dynamics, with model efficacy rigorously assessed through direct comparison of experimental and predicted outcomes (**Fig. 14b**). Validation analyses revealed that RF, GB, and XGB regressors exhibited a near-perfect predictive accuracy, achieving R^2 (0.99) with acceptable *MAE metrics*. However, the low *RMSE/MAE* value (0.9/0.7) for RF makes it the most practicable model for PWC without deposits (**Fig. 14c**). These results underscore the robustness of the RF model in simulating the corrosion response of deposit-free welded CS specimens under the specified conditions. A comprehensive tabulation of all ML models' performance parameters of welded CS samples without deposits is provided (**Table 3**).

The cumulative correlation matrix analysis of welded CS samples with SiO_2 deposit, i.e., CS-BM-SiO_2, CS-WM-SiO_2, and CS-HAZ-SiO_2, under sour conditions, without/with CRW11 inhibitor, enabled dataset integration into multiple ML algorithms (**Fig. 14d**). Comparative evaluation of predicted versus actual corrosion outcomes (**Fig. 14e**) identified all ML regressors (i.e., LR, RF, GB, DT, and XGBoost) as viable models with maximal R^2 (0.99) value, but DT demonstrated superior predictive accuracy, evidenced by its least RMSE/MAE errors (0.5/0.2) (**Fig. 14f**). Quantitative metrics confirmed DT regressors' efficacy in modeling corrosion behavior of SiO_2-deposited welded CS systems in sour environments, irrespective of CRW11 presence

(**Table 3**). These results advance predictive frameworks for corrosion science, offering actionable insights for material optimization and inhibitor-based mitigation strategies in sour-service industrial applications.

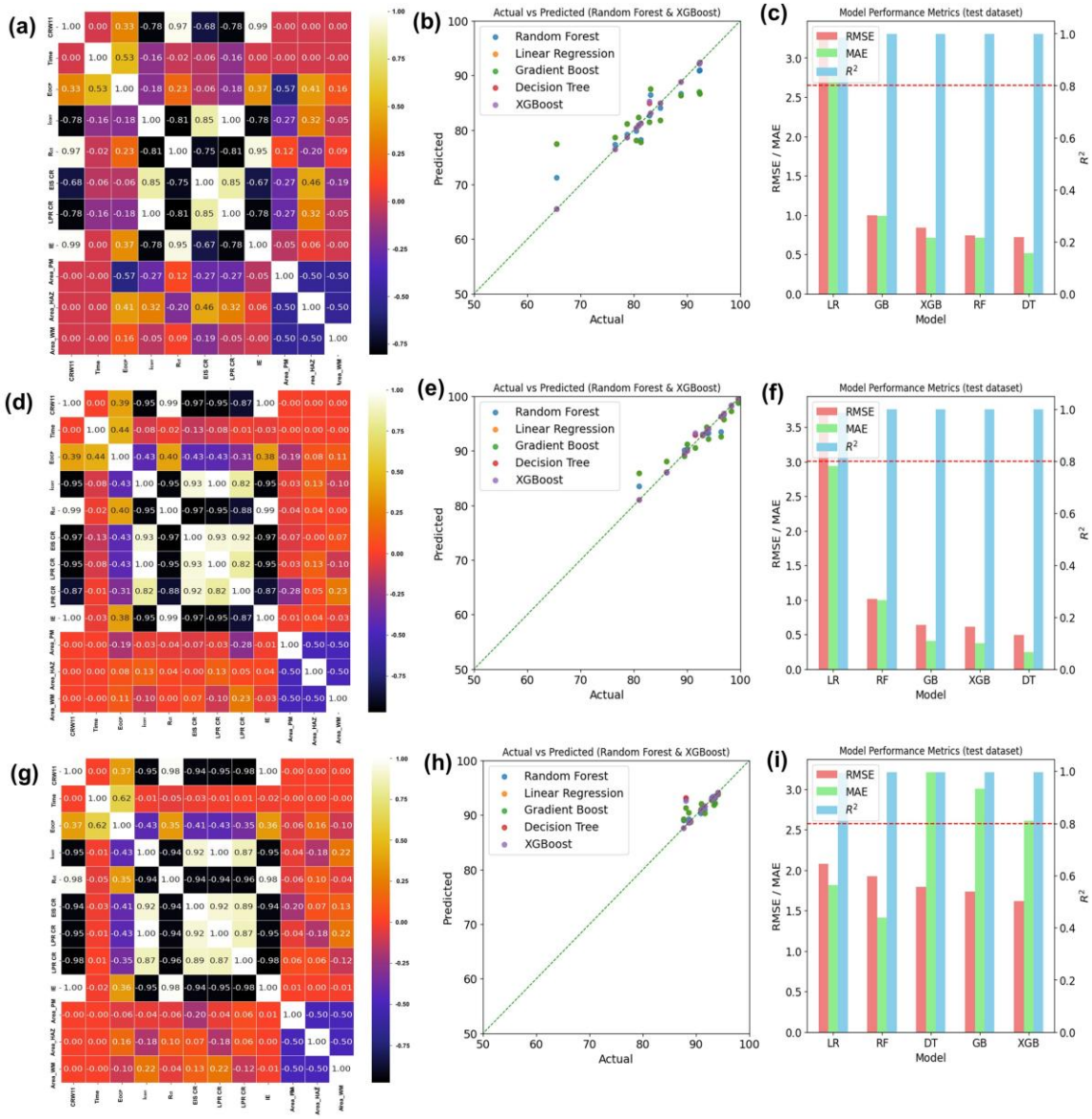

Fig. 14: Correlation matrix of entire dataset, comparison of actual vs. predicted IE% using LR, RF, DT, GB, and XGB regressors, and Models performance metrics for testing datasets of (a-c) welded CS, (d-f) welded CS + SiO_2 deposit and (g-i) welded CS + $CaCO_3$ deposit in absence/presence of CRW11 inhibitor in sour conditions.

A comprehensive study was conducted to investigate the corrosion behavior of welded CS samples with $CaCO_3$ deposits under sour conditions, without/with the CRW11 inhibitor. The

analysis focused on three sample types: CS-BM-$CaCO_3$, CS-WM-$CaCO_3$, and CS-HAZ-$CaCO_3$. A cumulative correlation matrix was employed to integrate the dataset into machine learning (ML) algorithms, enabling the development of predictive models (**Fig. 14g**). Although all ML regressors (i.e., RF, LR, DT, GB, and XGB) demonstrated possible performance with regards to optimal R^2 value (0.99), DT had insignificant *RMSE*/*MAE* (0.2/01) (**Fig. 14i**). These findings highlight the effectiveness of DT in predicting corrosion behavior with $CaCO_3$ deposits under sour conditions. Comparative performance metrics provide a basis for selecting optimal algorithms and advancing understanding of corrosion phenomena in welded CS samples with $CaCO_3$ deposits (**Table 3**). This work contributes to predictive modeling in corrosion science, with implications for materials selection, mitigation strategies, and risk assessment in sour environments.

Table 3: Summary of ML algorithms performance metrics for welded CS samples, without/with deposits (SiO_2 or $CaCO_3$) in presence of CRW11 inhibitor in sour conditions.

ML models	Test data metrics (No deposit)			Test data metrics (with SiO_2 deposit)			Test data metrics (with $CaCO_3$ deposit)		
	R^2	RMSE	MAE	R^2	RMSE	MAE	R^2	RMSE	MAE
LR	0.93	7.2	4.8	0.99	3.4	3.0	0.99	2.4	2.1
RF	0.99	0.9	0.7	0.99	1.2	0.7	0.99	1.1	1.4
GB	0.99	3.3	1.2	0.99	0.7	0.2	0.99	0.5	0.2
DT	0.98	3.4	1.2	0.99	0.5	0.2	0.99	0.2	0.1
XGBoost	0.99	3.1	1.1	0.99	0.9	0.3	0.99	1.0	0.3

4. Conclusions

This study thoroughly examined PWC and pitting corrosion in X65 welded CS pipelines subjected to sour circumstances, with an emphasis on the impacts of microstructures, elemental compositions, and inorganic deposits (SiO_2 or $CaCO_3$). The main findings of this work are summarized as follows:

- Electrochemical experiments revealed that SiO_2 deposits produced the highest CRs, in the order of CS-HAZ-SiO_2 (0.93–1.07mmpy) > CS-PM-SiO_2 (0.63–1.01mmpy) > CS-WM-SiO_2 (0.47–0.81mmpy), particularly from EIS and LPR analysis, compared to $CaCO_3$-deposited samples and un-deposited counterparts. However, the HAZ region in the absence of deposits

appears the most susceptible to corrosion in sour media, due to its granular fine bainite microstructures that enable rapid oxidation of Fe.

- ❖ The SiO_2 or $CaCO_3$ deposits increase aggressive species and stabilize iron oxides, regarding microstructural, compositional analyses and corrosion products confirmed by EDX, SEM, OM, and Raman spectra.
- ❖ An amine-based CRW11 inhibitor applied significantly reduced the CRs below the 0.1 mmpy industrially acceptable threshold, which was particularly beneficial for the CS-HAZ, the area most susceptible to PWC, thereby forming protective layers and scavenging oxygen in mitigative microgalvanic coupling.
- ❖ Artificial pit measurements revealed that the CS-PM-$CaCO_3$ exhibited the highest calculated pit depth (68.3 ± 2.7 μm) and pit propagation rate (1.2 ± 0.2 mmpy), making it the most vulnerable region to pitting relative to CS-WM-$CaCO_3$ (52.5 ± 1.1 μm; 0.9 ± 0.1 mmpy) and CS-HAZ-$CaCO_3$ (29.3 ± 0.6 μm; 0.5 ± 0.1). Also, exacerbated pitting corrosion was observed in CS-PM-SiO_2, amongst all the studied regions of welded CS without/with deposits, regarding its high actual pit depth. However, CS-WM-SiO_2 and CS-HAZ-SiO_2 are most affected by increased pit densities. This proves that SiO_2/$CaCO_3$ deposits on welded CS created a physical barrier for the surface nucleation effect and improved anodic dissolution.
- ❖ Machine learning models (RF, DT, GB, and XGB) were able to accurately predict IE with R^2 (0.99). Notably, RF is the most practicable ML model for tests without deposits at least RMSE (0.9), while DT is ideal for tests with SiO_2/$CaCO_3$ deposits at the lowest *RMSE* (0.5/0.2).
- ❖ Overall, this study advances the practical understanding of PWC and pitting corrosion of welded CS pipelines in sour conditions, offering valuable insights for the oil and gas sector's material selection, inhibitor use, and pipeline integrity control.

Data availability

The data supporting this article have been included as part of the ESI.†

CRediT authorship contribution statement

AKI: Writing – original draft, Methodology, Investigation, Data curation. **MHS**: Methodology, Investigation, Data curation. **DA**: Methodology, Investigation, Validation, Funding acquisition. **NL**: Methodology, Investigation, Validation, Supervision, Funding acquisition. **AR**: Writing –

original draft, Methodology, Data curation, Investigation. **PKY**: Methodology, Investigation, Validation, Supervision. **AMA**: Writing – review & editing, Supervision, Funding acquisition, Conceptualization.

Declaration

The authors do not have any conflict to declare.

Acknowledgements

This study was financially supported by the Academic Research Grant (ARG01-0524-230330) from the Qatar National Research Fund (QNRF), a member of the Qatar Foundation. The authors also acknowledge financial support from the Qatar Shell Research and Technology Centre. Additionally, the Central Laboratory Unit (CLU) at Qatar University provided SEM, EDX, and elemental mapping services. All statements in this work are the sole responsibility of the authors.

References

Abdullah, A.M., Fayyad, E. M., Ipadeola, A.K., Sliem, M.H., Abdeen, Dana, Al-Qahtani, N., RajKumar, Ashwin, Jeffrey J., Yalavarthy, P., 2025. Electrochemical and Machine Learning Analysis Unveils Protective Mechanisms of Commercial Amine-Based Inhibitors for Under-Deposit Corrosion of Carbon Steel in Sour Media. In: 248th Electrochemical Society (ECS) Meeting.

Abdulstaar, M., Mhaede, M., Wagner, L., 2013. Pre-Corrosion and Surface Treatments Effects on the Fatigue Life of AA6082 T6. Adv. Eng. Mater. 15(10), 1002-1006.

Adegbite, M.A., 2014. Flow accelerated preferential weld corrosion of X65 steel in brine. Cranfield University.

Al-Amiery, A.A., Isahak, W.N.R.W., Al-Azzawi, W.K., 2023. Corrosion inhibitors: natural and synthetic organic inhibitors. Lubricants 11(4), 174.

Al-Amiery, A.A., Mohamad, A.B., Kadhum, A.A.H., Shaker, L.M., Isahak, W.N.R.W., Takriff, M.S., 2022. Experimental and theoretical study on the corrosion inhibition of mild steel by nonanedioic acid derivative in hydrochloric acid solution. Sci. Rep. 12(1), 4705.

Alawadhi, K., Robinson, M., 2011. Preferential weld corrosion of X65 pipeline steel in flowing brines containing carbon dioxide. Corros. Eng. Sci. Technol. 46(4), 318-329.

Aljohani, T.A., Alateyah, A.I., El-Sanabary, S. and El-Garaihy, W.H., 2023. Chapter 16 - Corrosion of weldments. In: F. Khoshnaw (Editor), Welding of Metallic Materials. Elsevier, pp. 565-588. DOI: 10.1016/B978-0-323-90552-7.00010-9.40.

Anita, N., Joany, R.M., Dorothy, R., Aslam, J., Rajendran, S., Subramania, A., Singh, G., Verma, C., 2023. Chapter 4-Linear polarization resistance (LPR) technique for corrosion

measurements, Electrochemical and Analytical Techniques for Sustainable Corrosion Monitoring. Chapter 4 Elsevier, pp. 59-80. DOI: 10.1016/B978-0-443-15783-7.00005-0.

Aslam, R., Mobin, M., Zehra, S., Aslam, J., 2022. A comprehensive review of corrosion inhibitors employed to mitigate stainless steel corrosion in different environments. J. Mol. Liq. 364, 119992.

Aydinsoy, E.A., Aghamaliyev, Z.Z., Aghamaliyeva, D.B., Abbasov, V.B., 2024. A systematic review of corrosion inhibitors in marine environments: Insights from the last 5 years. Process. Petrochem. OI. 25(3), 793-843.

Baranwal, P.K., Rajaraman, P.V., 2019. Electrochemical investigation on effect of sodium thiosulfate (Na2S2O3) and ammonium chloride (NH4Cl) on carbon steel corrosion. J. Mater. Res. Technol. 8(1), 1366-1378.

Behvar, A., Haghshenas, M., Djukic, M.B., 2024. Hydrogen embrittlement and hydrogen-induced crack initiation in additively manufactured metals: A critical review on mechanical and cyclic loading. Int. J. Hydrog. Energy 58, 1214-1239.

Bleij, A., Ponomareva, M., Nadlinger, M., Schimo-Aichhorn, G., Bingemann, D., Rathmell, C., Luckeneder, G., Haslehner, G., Gattinger, P., Brandstetter, M., 2022. In situ Raman Spectroscopy Monitors the Corrosion of Mild Steel in a Salt Fog Chamber. Spectrosc. 37, 8-18.

Bonzom, R., Oltra, R., 2016. Intergranular corrosion propagation rate of 2024 alloy investigated via the “one- dimensional artificial pit” technique. Corros. Sci. 111, 850-855.

Butler, K.T., Davies, D.W., Cartwright, H., Isayev, O., Walsh, A., 2018. Machine learning for molecular and materials science. Nature 559, 547-555.

Case, R., Achour, M., Daniels, J., 2015. Evaluation of preferential weld corrosion susceptibility and its mitigation in slightly sour conditions, NACE Corrosion, 2015-5640.

Chan, W.M.M., 2003. A critical study on corrosion and corrosion control methods for piping systems in Hong Kong. Hong Kong Polytechnic University (Hong Kong).

Chen, L., Lu, D., Zhang, Y., 2022. Organic compounds as corrosion inhibitors for carbon steel in HCl solution: a comprehensive review. Materials 15, 2023.

Chen, T., Guestrin, C., 2016. Xgboost: A scalable tree boosting system. In: Proceedings of the 22nd acm sigkdd international conference on knowledge discovery and data mining, pp. 785-794.

Cheng, W., Luo, S., Chen, Y., 2019. Use of EIS, Polarization and Electrochemical Noise Measurements to Monitor the Copper Corrosion in chloride media at different temperatures. Int. J. Electrochem. Sci. 14(5), 4254-4263.

Choi, Y.Y., Kim, M.H., 2018. Corrosion behaviour of welded low-carbon steel in the Arctic marine environment. RSC Adv. 8(53), 30155-30162.

Coelho, L.B., Zhang, D., Van Ingelgem, Y., Steckelmacher, D., Nowé, A., Terryn, H., 2022. Reviewing machine learning of corrosion prediction in a data-oriented perspective. Npj Mater. Degrad. 6, 8.

Colomban, P., Slodczyk, A., 2009. Raman intensity: An important tool in the study of nanomaterials and nanostructures. Acta Phys. Pol. A 116, 7-12.

Da Silva, C.A., 2023. Corrosion in multiphase-flow pipelines: the impact on the oil and gas industry. DOI: 10.11606/T.3.2023.tde-17072023-091725.

Diao, Y., Yan, L., Gao, K., 2021. Improvement of the machine learning-based corrosion rate prediction model through the optimization of input features. Mater. Des. 198, 109326.

Dong, Y., Liu, D., Du, H., Sun, H., Zuo, X., 2023. Effect of microstructure on the mechanical properties and corrosion resistance of a welded joint of 620-grade marine steel. Front. Mater. 10, 1107125.

Dong, Z., Ding, L., Meng, Z., Xu, K., Mao, Y., Chen, X., Ye, H., Poursaee, A., 2024. Machine learning-based corrosion rate prediction of steel embedded in soil. Sci. Rep. 14, 18194.

Dwivedi, D., Lepková, K., Becker, T., 2017. Carbon steel corrosion: a review of key properties and characterization methods. RSC Adv. 7(8), 4580-4610.

Fakheri, M., Zare, H.R., Mohammadpour, Z., Mosallaee, M., 2020. The impact of Ni on the corrosion behavior and microstructure of weld metal fabricated from E8018-G electrodes. Weld. World 64(6), 1065-1075.

Fayyad, E.M., Ipadeola, A.K., Sliem, M.H., Abdeen, D., Al-Qahtani, N., RajKumar, A., Jeffrey, J., Yalavarthy, P.K., Abdullah, A.M., 2025. Interfacial robustness of commercial amine-based inhibitors mitigates under-deposit corrosion of carbon steel in simulated sour conditions: a merged electrochemical and machine learning study. Emergent Mater, doi.org/10.1007/s42247-025-01196-4.

Gapsari, F., Darmadi, D.B., Seyarini, P.H., Izzuddin, H., Madurani, K., Tanji, A., Haermawan, H., 2021. Nephelium lappaceum Extract as an Organic Inhibitor to Control the Corrosion of Carbon Steel Weldment in the Acidic Environment. Sustainability 13(21), 12135.

Han, J., 2009. Galvanic mechanism of localized corrosion for mild steel in carbon dioxide environments. Ohio University.

Heuer, J., Luttge, A., 2018. Kinetics of pipeline steel corrosion studied by Raman spectroscopy-coupled vertical scanning interferometry. Npj Mater. degrad. 2(1), 40.

Ipadeola, A.K., Eid, K., Abdullah, A.M., Al-Hajri, R.S., Ozoemena, K.I., 2022. Pd/Ni-metal–organic framework-derived porous carbon nanosheets for efficient CO oxidation over a wide pH range. Nanoscale Adv. 4(23), 5044-5055.

Ipadeola, A.K., Haruna, A.B., Abdullah, A.M., Al-Hajri, R.S., Viter, R., Ozoemena, K.I., Eid, K., 2023a. Ternary PdNiO nanocrystals-ornamented porous CeO2/onionlike carbon for electrooxidation of carbon monoxide: unveiling the effect of supports and electrolytes. Catal. Sci. Technol. 13(10), 3035-3046.

Ipadeola, A.K., Haruna, A.B., Abdullah, A.M., Shibl, M.F., Ahmadaliev, D., Ozoemena, K.I., Eid, K., 2023b. Electrocatalytic CO oxidation on porous ternary PdNiOCeO2/carbon black nanocatalysts: Effect of supports and electrolytes. Catal. Today 421, 114178.

Ipadeola, A.K. Sliem, M.H., Abdeen, D., Laycock, N., RajKumar, A., Yalavarthy, P. K., Abdullah, A. M., 2025. Unmasking the Hidden Threat: Conductive Under-Deposits and Their Role

in Preferential Weldment Corrosion of Carbon Steel under Sour Conditions. Langmuir 41(35), 23632–23651.
Jamali, S.S., Mills, D.J., 2016. A critical review of electrochemical noise measurement as a tool for evaluation of organic coatings. Prog. Org. Coat. 95, 26-37.
Jáquez-Muñoz, J.M., Gaona-Tiburcio, C., Méndez-Ramírez, C.T., Martínez-Ramos, C., Baltazar-Zamora, M.A., Santiago-Hurtado, G., Estupinan-Lopez, F., Landa-Ruiz, L., Nieves-Mendoza, D., Almeraya-Calderon, F., 2024. Electrochemical Noise Analysis: An Approach to the Effectivity of Each Method in Different Materials. Materials 17(16), 4013.
Jun, J., Li, T., Frankel, G., Sridhar, N., 2020. Corrosion and repassivation of Super 13Cr stainless steel in artificial 1D pit electrodes at elevated temperature. Corros. Sci. 173, 108754.
Jung, K.-H., Lee, J.-H., 2024. Prediction of Corrosion Rate for Carbon Steel Using Regression Model with Commercial LPR Sensor Data. Appl. Sci. 14(23), 10836.
Kappes, M., Frankel, G., Sridhar, N., Carranza, R., 2012. Reaction paths of thiosulfate during corrosion of carbon steel in acidified brines. J. Electrochem. Soc. 159(4), C195.
Katiyar, P.K., Maurya, R., Singh, P.K., 2022. Highlighting the corrosion mechanisms of corroded plain carbon steels using the atomic force microscopy. Int. J. Sustain. Build. Technol. Urban Dev. 13(2), 198-220.
Ko, S.-J., An, J.-H., Kim, Y.-S., Kim, W.-C., Kim, J.-G., 2019. Effects of corrosion on mechanical properties of welded carbon steel pipe in district heating water. Materials 12(22), 3682.
Kolli, S., Javaheri, V., Kömi, J. Porter, D., 2019. On the role of grain size and carbon content on the sensitization and desensitization behavior of 301 austenitic stainless steel. Metals 9(11), 1193.
Lahiri, A.K., 2017. Metallurgical Aspects of Welding, Applied Metallurgy and Corrosion Control: A Handbook for the Petrochemical Industry. Springer Singapore, Singapore, pp. 141-176. DOI: 10.1007/978-981-10-4684-1_7.
Li, B., Xia, Q., Dong, W., 2025. Comparative Study of the Corrosive Behaviors of Rust Layers on Bronze Ware in Different Corrosive Environments. Materials 18(6), 1359.
Li, W., Cao, R., Xu, L., Qiao, L., 2021. The role of hydrogen in the corrosion and cracking of steels - a review. Corros. Commun. 4, 23-32.
Liu, J., Wang, B., Chen, T., Hao, L., Wu, J., Liu, C., 2025. The Effect of Corrosion Inhibitors on the Corrosion Behavior of Ductile Cast Iron. Metals 15(1), 70.
Lu, Y., Jing, H., Han, Y., Xu, L., 2016. Effect of Welding Heat Input on the Corrosion Resistance of Carbon Steel Weld Metal. J. Mater. Eng. Perform. 25(2), 565-576.
Martin, M.L., Sofronis, P., 2022. Hydrogen-induced cracking and blistering in steels: A review. J. Nat. Gas Sci. Eng. 101, 104547.
Miksic, B.M., Furman, A.Y., Kharshan, M.A., 2009. Effectiveness of the corrosion inhibitors for the petroleum industry under various flow conditions, NACE Corrosion, NACE-09573.
Natesan, M., Selvaraj, S., Manickam, T., Venkatachari, G., 2008. Corrosion behavior of metals and alloys in marine-industrial environment. Sci. Technol. Adv. Mater. 9(4), 045002.

Nguyen, T.C., So, Y.S., Yoo, J.S., Kim, J.G., 2022. Machine learning modeling of predictive external corrosion rates of spent nuclear fuel carbon steel canister in soil. Sci. Rep. 12(1), 20281.

Nik Mohamed Daud, N.M.R., Eng, K.K, Jumbri, K. Nor, A.M., Suhor, M.F., Borhan, N., Abas, A.Z., Aizamddin, M.F., Mohd Pu'ad, M.J., Muhammad M.F., 2023. Benchmarking the impact of nickel filler addition, weld hardness, environmental pH, and corrosion inhibitors on A333 carbon steel pipe weld corrosion. Results Eng. 20, 101633.

Niu, G., Yuan, R., Wang, E., Yang, X., Liu, Z., Li, Z., Zhang, Z., Gong, N., Li, K., Su, B., Zhang, J., Wu, H., Li, X., Murr, L.E., 2024. Unraveling the influence of Mo on the corrosion mechanism of Ni-advanced weathering steel in harsh marine atmospheric environments. J. Mater. Sci. Technol. 195, 41-62.

Nofrizal, N., Robinson, M., Impey, S., 2016. The Effect of Flow Rate on the Preferential Weld Corrosion of X65 Pipeline Steel. Eur. Corros. Congr. EUROCOR, 4, 2374À2385.

Orhorhoro, E.K., Erameh, A.A., Tamuno, R.I., 2022. Investigation of the effect of corrosion rate on post welded heat treatment of medium carbon steel in seawater. J. Appl. Res. Ind. Eng. 9(1), 59-67.

Palumbo, G., Dunikowski, D., Wirecka, R., Mazur, T., Lelek-Borkowska, U., Wawer, K., Banaś, J., 2021. Effect of grain size on the corrosion behavior of Fe-3wt.% Si-1wt.% Al electrical steels in pure water saturated with CO2. Materials 14(17), 5084.

Paolinelli, L.D., Pérez, T., Simison, S.N., 2008. The effect of pre-corrosion and steel microstructure on inhibitor performance in CO2 corrosion. Corros. Sci. 50(9), 2456-2464.

Park, J.S., Lee, J.W., Kim, S.J., 2021. Hydrogen-induced cracking caused by galvanic corrosion of steel weld in a sour environment. Materials 14(18), 5282.

Pessu, F.O., Saleem, E., Espejo, C., Neville, A., 2022. Understanding the local pitting corrosion characteristics of carbon steel in CO2 corrosion environment using artificially machined pits. Results Eng. 16, 100700.

Răuță, D.-I., Matei, E., Avramescu, S.-M., 2025. Recent Development of Corrosion Inhibitors: Types, Mechanisms, Electrochemical Behavior, Efficiency, and Environmental Impact. Technologies 13(3), 103.

Ribeiro, D.V., Souza, C.A.C., Abrantes, J.C.C., 2015. Use of Electrochemical Impedance Spectroscopy (EIS) to monitoring the corrosion of reinforced concrete. Rev. IBRACON Estrut. Mater. 8, 529-546.

Rizzo, R., Gupta, S., Rogowska, M., Ambat, R., 2020. Corrosion of carbon steel under CO2 conditions: Effect of CaCO3 precipitation on the stability of the FeCO3 protective layer. Corros. Sci. 162, 108214.

Ruiz, D., Casas, A., Escobar, C.A., Perez, A., Gonzalez, V., 2024. Advanced Machine Learning Techniques for Corrosion Rate Estimation and Prediction in Industrial Cooling Water Pipelines. Sensors 24(11), 3564.

Samusawa, I., Shimamura, J., Al Helal, A. and Sapanathan, T., 2025. Novel Insights into Trenching of Ni-Containing Low Alloy Steel in Simulated Sour Conditions with Sodium Thiosulfate. Corrosion 81(2), 182-193.

Santa, A.C.., Montoya, D.A., Tamayo, J.A., Gómez, M.A., Castaño, J.G., Baena, L.M., 2024. Atmospheric corrosion of carbon steel: Results of one-year exposure in an andean tropical atmosphere in Colombia. Heliyon 10(8), e29391.

Song, L., Peng, Y., Zhao, H., Cao, Y., Fang, Q., 2022. Corrosion resistance analysis of the weld metal of low-alloy high-strength steel considering different alloy compositions. Front. Mater. 9, 957669.

Sun, J., Tang, H., Wang, C., Han, Z., Li, S., 2022. Effects of Alloying Elements and Microstructure on Stainless Steel Corrosion: A Review. Steel Res. Int. 93(5), 2100450.

Surnam, B.Y.R., Chui, C.-W., Xiao, H., Liang, H., 2016. Investigating atmospheric corrosion behavior of carbon steel in coastal regions of Mauritius using Raman Spectroscopy. Matéria (Rio J.) 21(1), 157-168.

Talukdar, A., Rajaraman, P.V., 2020. Investigation of acetic acid effect on carbon steel corrosion in CO2–H2S medium: mechanistic reaction pathway and kinetics. ACS Omega 5(20), 11378-11388.

Tan, M.Y., 2022. Chapter 6-Localized Corrosion Impacted by Flow and Erosion, Localized Corrosion in Complex Environments. Wiley, pp. 249-297.

Ura-Bińczyk, E., Dobkowska, A., Andrzejczuk, M., Roguska, A., Mazurkiewicz, B., Solarski, W., Balcer, M., Lewandowska, M., Banaś, J., 2021. Application of LPR and EIS techniques for on-site corrosion monitoring at the geothermal plant in Central Poland. Mater. Corros. 72(9), 1518-1528.

Usman, B.J., Gasem, Z.M., Umoren, S.A., Solomon, M.M., 2019. Eco-friendly 2-Thiobarbituric acid as a corrosion inhibitor for API 5L X60 steel in simulated sweet oilfield environment: Electrochemical and surface analysis studies. Sci. Rep. 9(1), 830.

Weber, J., Starchenko, V., Ilavsky, J., Allard, L.F., Mata, J., Debeer-Schmitt, L., Cooke, C.G., Littrell, K., He, L., Zhang, R., 2023. Grain boundary widening controls siderite (FeCO3) replacement of limestone (CaCO3). Sci. Rep. 13(1), 4581.

Xijing, L., Yong, C., 2023. Effect of SiO2 nanoparticles on the hardness and corrosion resistance of NiW/SiO2 nano composite coating prepared by electrodeposition. Int. J. Electrochem. Sci. 18(6), 100138.

Xiong, Q., Hu, J., Gu, C., Feng, M., Zhang, Z., Zhong, X., 2020. The study of under deposit corrosion of carbon steel in the flowback water during shale gas production. Appl. Surf. Sci. 523, 146534.

Xu, Y., Liu, L., Zhou, Q., Wang, X., Huang, Y., 2020. Understanding the influences of pre-corrosion on the erosion-corrosion performance of pipeline steel. Wear 442, 203151.

Yahya, S., Othman, N., Daud, A., Jalar, A., 2013. Surface morphology studies of low carbon steel treated in aqueous lignin. Sains Malays. 42, 1793-1798.

Yang, L., 2020. Techniques for corrosion monitoring. Woodhead Publishing.

Yang, L, Ma, Z., Zheng, Y., Wang, X., Huang, Y., Wang, K., Song, S., Jin, W., 2021. The Study of Corrosion Behaviors of Carbon Steel Weldments and Their Inhibition in Simulated Pore Solution Using Multi-Electrode Array Technique. Appl. Sci. 11(18), 8278.

Zhang, S., Bian, T., Yu, H., Wu, P., Mou, L., Liu, B., Hou, L, Wei, Y., Zhang, Y., 2024. New insights on the effect of chloride concentrations and Mo alloying on corrosion behavior of 3Cr steel in CO2 environments. Mater. Today Commun. 40, 109448.

Zhang, S., Zhao, H., Shu, F., He, W., Wang, G., 2017. Microstructure and corrosion behavior of simulated welding HAZ of Q315NS steel in sulfuric acid solution. Metals 7(6), 194.

Zhang, Z., Studer, P., Angst, U., 2022. A multi-technique study of corrosion products at the steel-concrete interface under two exposure conditions. J Microsc. 286(2), 191-197.